

# Susceptibility of copper to pitting corrosion in bicarbonate buffer solutions: Part I. Effect of chloride

James Noël (✉ [jjnoel@uwo.ca](mailto:jjnoel@uwo.ca))

Western University

Sina Matin

Western University <https://orcid.org/0000-0002-5339-9313>

Jeffrey Henderson

Surface Science Western <https://orcid.org/0000-0001-7415-756X>

Mark Biesinger

Surface Science Western

Brad Kobe

Surface Science Western

David W. Shoesmith

Western University

---

## Article

### Keywords:

**Posted Date:** January 25th, 2023

**DOI:** <https://doi.org/10.21203/rs.3.rs-2436748/v1>

**License:**   This work is licensed under a Creative Commons Attribution 4.0 International License.

[Read Full License](#)

**Additional Declarations:** (Not answered)

---

# Susceptibility of copper to pitting corrosion in bicarbonate buffer solutions: Part I. Effect of chloride

Sina Matin<sup>1</sup>, Jeffrey D. Henderson<sup>2</sup>, Mark Biesinger<sup>1,2</sup>, Brad Kobe<sup>2</sup>, David W. Shoesmith<sup>1,2</sup>, James J. Noël<sup>1,2</sup>

1. Department of Chemistry, Western University, London, Canada
2. Surface Science Western, Western University, London, Canada

## Abstract

The pitting corrosion, passive film morphology, and surface composition of copper were studied in chloride-containing bicarbonate buffer solutions using multielectrode arrays and single electrodes. Cu was shown to be susceptible to pitting in 0.01 and 0.1 M Cl<sup>-</sup>, but to experience active dissolution in 1 M Cl<sup>-</sup>. The passive film morphology and composition were investigated using the single-electrode setup. Surface analyses showed the presence of pits in both 0.01 and 0.1 M Cl<sup>-</sup> buffer solutions. The results indicated the dependency of passive film morphology and composition on both charge density and applied potential.

## 1. Introduction

Copper and copper alloys are used in various industries including oil and gas, marine, construction, and nuclear. Different types of oxide films can be formed on a Cu surface depending on the environment to which it is exposed. As a result, Cu oxides may have either a positive or negative influence on corrosion performance in specific applications. For instance, the formation of corrosion products can decrease the efficiency of a cooling system by inducing a lower heat transfer rate. Additionally, an oxide layer may protect the base metal from further degradation in corrosive environments or, if unstable in harsh environments, result in unpredictable material failures<sup>1-10</sup>.

Some metals form a thin, dense, and uniform oxide film on the surface, commonly referred to as a passive film, which protects them from further dissolution. Two different mechanisms have been proposed for protective film formation: (1) metal dissolution as cations followed by their precipitation as oxides or/and hydroxides on the metal surface (dissolution-precipitation mechanism)<sup>11-13</sup>; and (2) nucleation and growth of a passive film via a solid-state reaction<sup>12,14</sup>. The morphology and properties of oxide films depend on parameters such as applied potential, solution composition, grain orientation, and exposure time<sup>12,14-26</sup>. For instance, the formation of passive films on Cu in moderately alkaline solutions leads to a dual layer film structure with

inner  $\text{Cu}_2\text{O}$  and outer  $\text{CuO}$  or/and  $\text{Cu}(\text{OH})_2$  layers<sup>12,22,27-29</sup>. The  $\text{Cu}_2\text{O}$  is commonly porous, allowing  $\text{Cu}^{2+}$  ions to diffuse into solution and precipitate to form an outer layer of  $\text{CuO}$  or/and  $\text{Cu}(\text{OH})_2$ . The properties of this double-layer film on the Cu surface depend on the pH of the solution<sup>12,17,30-32</sup>.

While the formation of a passive film will decrease the general corrosion rate, any localized damage to the film can result in accelerated corrosion rates at discrete locations. Pitting is a common form of localized corrosion, and a major concern due to its unpredictability, ability to penetrate the bulk material, and self-sustaining nature. Many studies have been conducted on the properties of passive films, such as their structure, composition, and thickness and their role in pitting<sup>4,8,33-46</sup>.

Two main mechanisms have been proposed to explain pitting: (1) mechanical breakdown of the passive film due to the transport of aggressive anions from the solution through the oxide film to produce a large interfacial stress at the metal surface<sup>47</sup>; and (2) local thinning of the passive film due to surface adsorption of aggressive anions from solution<sup>34,48</sup>. Defining the rate-determining step is of key importance in understanding the mechanism of pitting, and two rate-determining steps have been proposed: (1) passive film breakdown; and (2) the transition from metastable to stable pit growth. The role of passive film breakdown is negligible if the repassivation potential ( $E_{rp}$ ) is just below the breakdown potential ( $E_b$ ) when pit propagation will be slow, but breakdown becomes rate-determining when pitting occurs at relatively high potentials when the subsequent process of pit propagation will be rapid due to the resistivity of the passive film<sup>49</sup>. Pitting comprises a number of steps, including metastable initiation, a metastable-to-stable pitting transition, and stable pit growth. While a specific system might experience a large number of metastable pits, few of them are generally able to transition to stable pits.

Different parameters have been introduced to characterize stable pit growth, such as  $ix$ ,  $ir$ ,  $i\sqrt{t}$ , and  $i_{diss, max}$  where  $i$  is the pit current density,  $x$  is the pit depth in a 1D pit,  $r$  is the depth of a hemispherical pit,  $t$  is time, and  $i_{diss, max}$  is the maximum dissolution current density<sup>1,8,10,38,45</sup>. While Silverman<sup>50</sup> reported that the presence of a salt film at the base of a passive film breakdown site could prevent the transition from metastable to stable pit growth, Frankel<sup>39-42,51,52</sup> demonstrated that this transition could occur even in the presence of the salt film and that pit growth could be either a charge transfer- or diffusion-controlled process<sup>5,7,53</sup>.

A common method to determine the susceptibility of materials to pitting is to compare the corrosion potential ( $E_{\text{corr}}$ ) to  $E_b$  and  $E_{\text{rp}}$ <sup>29,54</sup>. However, these potentials are distributed parameters due to variations in surface properties, variations in the local environment at the metal surface, and the stochastic nature of passive film breakdown. Pitting becomes possible when  $E_{\text{corr}}$  is equal to or more positive than  $E_b$ <sup>29,54,55</sup>, and subsequently proceeds via four main steps: (1) initiation, (2) metastable growth, (3) stable growth, and (4) repassivation<sup>3,9,13</sup>. Pitting starts with the nucleation of pits on the surface of materials due to the breakdown of the passive film, with some of the metastable pits initially formed subsequently transitioning into stable pits. It is commonly accepted that the stability of a pit depends on the aggressiveness of the solution inside the pit<sup>2-8,36,37,39-42,56-61</sup>, with the concentration of this solution necessarily higher than a critical concentration ( $C_{\text{crit}}$ ) required to sustain active dissolution.

Anions can have a positive (e.g.,  $\text{CO}_3^{2-}$  and  $\text{OH}^-$ ) or a negative effect (e.g.,  $\text{Cl}^-$  and  $\text{SO}_4^{2-}$ ) on the stability of passive films, which will affect the key pitting parameters,  $E_{\text{corr}}$ ,  $E_b$ ,  $E_{\text{rp}}$ , and the critical pitting temperature (CPT). The CPT is defined as the lowest temperature required for the formation of stable pits in a given environment. When multiple anions are present, there is competition between the adsorption of aggressive and inhibiting anions on the oxide surface<sup>62,63</sup>. The aggressive anions,  $\text{Cl}^-$  and  $\text{SO}_4^{2-}$ , play a significant role in passive film breakdown and pit initiation<sup>53,55,64-66</sup>, while  $\text{CO}_3^{2-}$  exerts an inhibiting effect by increasing the stability of the passive film<sup>67</sup>. Some studies have proposed that the behaviour of aggressive anions varies<sup>62,64,68,69</sup>. For example,  $\text{Cl}^-$  ions can accelerate corrosion at relatively low concentrations but behave like inhibitors at higher concentrations, due to the rapid rate of  $\text{CuCl}$  formation on the surface once the solubility of  $\text{CuCl}$  has been reached<sup>64</sup>. Another factor that could affect the pitting probability of materials is the solution pH, with the dependency of the  $E_b$  on pH having been debated for decades<sup>62,70,71</sup>.

In general, three mechanisms have been proposed to explain the pitting of metals: the Salina-Bravo and Newman (SBN); the Point Defect (PDM); and the Li, Scully, and Frankel (LSF) models<sup>2,40-42,51,52,72</sup>. In the SBN model, it is proposed that a salt film exists on the metal surface inside the pit<sup>2</sup>. This film can be formed on the metal surface if the critical current density ( $i_{\text{crit}}$ ) increases to a value equal to or greater than the anodic limiting current density ( $i_L$ ) and then the pit will grow under diffusion control. The SBN model was not able to explain why the measured current density was lower than  $i_L$  while metastable-to-stable pit growth was observed. The PDM

proposed the mechanical breakdown of the passive film through the accumulation of cation vacancies at the metal/oxide interface by transport from the oxide/solution interface; however, other types of pitting mechanisms are not covered in this model. To overcome the limitations inherent to the SBN and PDM models, Frankel and coworkers<sup>39-42,51,52</sup> developed the LSF model. Based on the LSF model, passive film breakdown is the critical factor when metal is exposed to a less aggressive environment or the microstructure of the material is less susceptible to pitting. In this case, the rate of passive film breakdown is low, but when it occurs, the pit grows rapidly. On the other hand, when a material is exposed to an aggressive solution, pit growth becomes the critical factor, due to the high frequency of passive film breakdown events and the formation of a large number of metastable pits.

Cu and its alloys have been shown to be corrosion resistant in environments such as seawater and anoxic solutions. However, localized corrosion processes can occur under aerated conditions in the presence of aggressive anions, or when the pH of the solution is increased. Many studies have been performed to investigate the pitting of Cu in a range of environments, with corrosion parameters considered to be deterministic, not distributed<sup>18,22,26,27,29,31,54,65-67</sup>. However, we showed the stochastic nature of corrosion parameters in our previous papers<sup>73</sup>. Here, we investigate the pitting probability, passive film morphology, and composition of oxide films in solutions with different chloride concentrations, using electrochemical, surface analysis, and statistical techniques to determine the pitting mechanism of Cu.

## **2. Experimental Methodology**

### **2.1. Sample preparation**

O-free and P-doped wrought Cu were supplied by the Swedish Nuclear Fuel and Waste Management Company (SKB, Solna, Sweden). Electrodes were machined as either “bullets” (used in multielectrode arrays, Fig. 1) or as cylindrical samples (with a 10 mm diameter and 4 mm thickness, used in single-electrode experiments). Bullet samples were used to avoid edge effects during electrochemical experiments. For multielectrode experiments, Cu specimens were prepared by rotating at 2700 RPM while grinding with a sequence of SiC papers (P600, P800, P1200, P2500, and P4000). The specimens were then rinsed with Type I water (18.2 M $\Omega$ .cm) prepared using a Millipore Milli-Q plus system, sonicated in ethanol, and dried in a stream of Ar gas prior to each experiment.

For single-electrode experiments, cylindrical Cu samples were mounted in epoxy and subjected to a vacuum for 5 minutes to remove bubbles from the epoxy, and to avoid the formation of crevices between the sample and the epoxy. Cu specimens were ground with a sequence of SiC papers (P600, P800, P1200, P2500, and P4000), followed by a final polish using a 1  $\mu\text{m}$  diamond suspension, to achieve a mirror surface finish. Then, the samples were rinsed in Type I water, sonicated in ethanol and dried in a stream of Ar gas prior to each experiment.



**Fig. 1:** O-free and P-doped copper “bullet” electrodes.

## **2.2.Solution preparation**

Solutions were prepared with reagent-grade sodium chloride ( $\text{NaCl}$ , 99.0%), sodium carbonate ( $\text{Na}_2\text{CO}_3$ , 99.5%), and sodium bicarbonate ( $\text{NaHCO}_3$ , 99.7%) provided by Fisher Scientific, using Type I water. The solutions were composed of a 0.005 M  $\text{Na}_2\text{CO}_3/\text{NaHCO}_3$  buffer solution containing various concentrations of  $\text{NaCl}$  within the range from 0.01 M to 0.1 M. The pH of the solutions was adjusted to 9 using the 0.005 M  $\text{Na}_2\text{CO}_3/\text{NaHCO}_3$  buffer solution.

## **2.3.Electrochemical cell, instrumentation, and procedure**

All potentiodynamic and potentiostatic experiments were performed in a conventional three-electrode electrochemical cell using either 30 Cu bullets as working electrodes

(multielectrode arrays) or a single Cu working electrode, a Ti plate or Pt wire as the counter electrode, and a saturated calomel reference electrode (SCE, 0.242 V vs. SHE) as reference. In the multielectrode array experiments, the counter electrode had a surface area of 200 cm<sup>2</sup>, and was just smaller than the cell bottom. The electrochemical cell was placed inside a Faraday cage to reduce electrical noise from external sources.

### 2.3.1. Multielectrode arrays

Corrosion potential ( $E_{\text{corr}}$ ) and potentiodynamic polarization experiments were conducted using a Multichannel Microelectrode Analyzer 910 (MMA, Scribner Associates) connected to a computer equipped with MMAlive software. The instrument was equipped with five 100  $\mu\text{A}$  zero resistance ammeters (ZRA). Fig. 2 shows a schematic of the instrument and multielectrode array used. In potentiodynamic experiments only the positive-going scan was conducted to measure  $E_b$ . Prior to the scan, electrodes were cathodically cleaned at -0.85 V vs SCE for 3 minutes to reduce any air-formed oxides. Then,  $E_{\text{corr}}$  was monitored for 30 minutes to allow a steady-state condition to be established and to determine the range of  $E_{\text{corr}}$  values on the multielectrode array. The potential was then scanned from  $E_{\text{corr}}$  in the positive direction at a scan rate of 10 mV/min until the current on all electrodes reached 100  $\mu\text{A}$ , followed by a negative-going scan at the same scan rate as the positive-going scan until all currents reached the passive current density. A schematic of the positive-going scan is shown in Fig. 3. Histograms of  $E_{\text{corr}}$  and  $E_b$  determined under passive conditions were plotted to facilitate the selection of applied potentials to be used in potentiostatic experiments. The applied potentials for potentiostatic experiments were chosen to be a) the maximum observed  $E_{\text{corr}}$  value + 20 mV and b) the minimum observed  $E_b$  value - 20 mV. These values were chosen to cover the tails of the  $E_{\text{corr}}$  and  $E_b$  distribution curves where there are concerns about the pitting probability<sup>73</sup>.

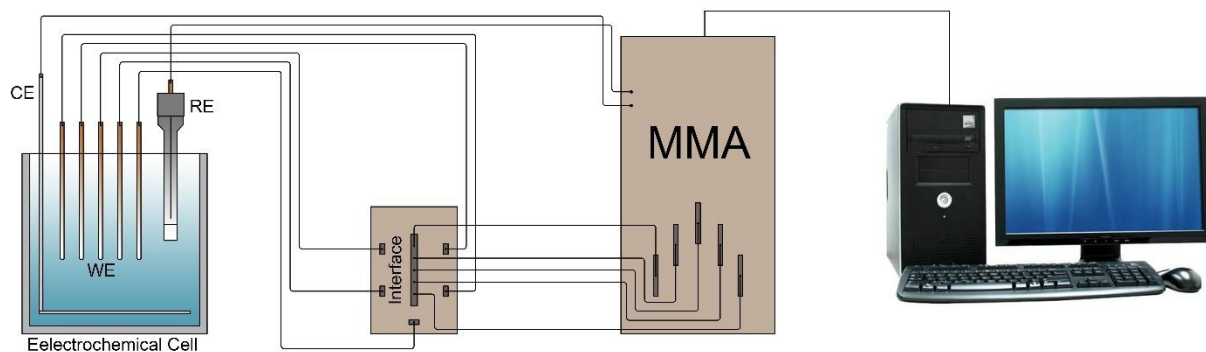


**Fig. 2:** Schematic of Multichannel Microelectrode Analyzer (MMA) connected to a multielectrode array.

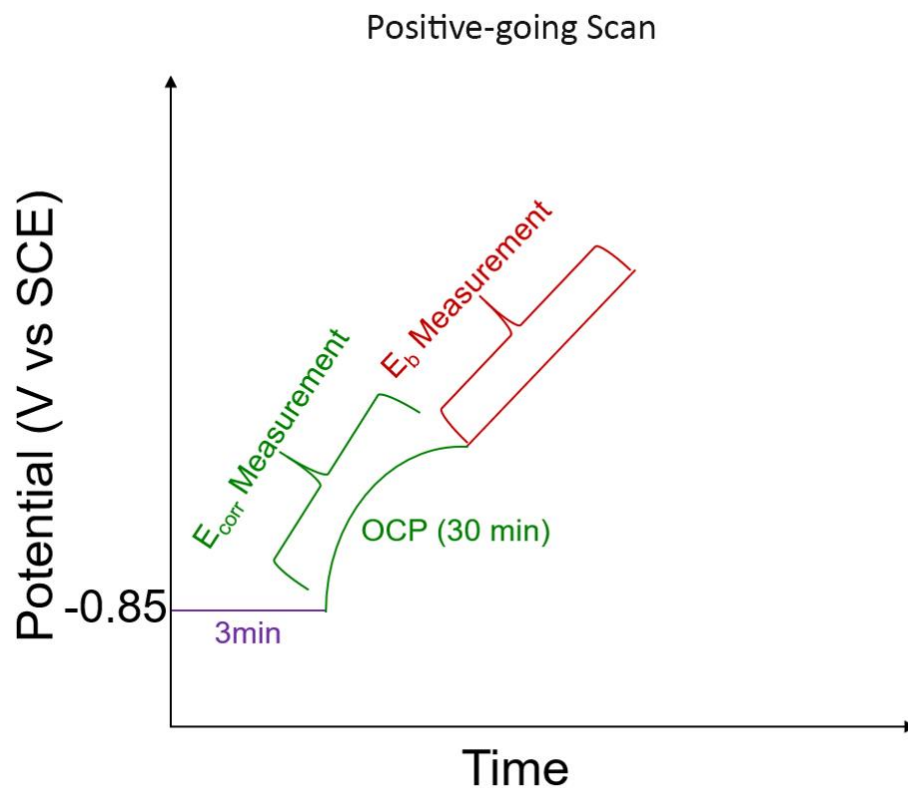


**Fig 3:** Schematic of the potential profile used to measure  $E_{\text{corr}}$  and, in potentiodynamic experiments, to measure  $E_b$ .

$E_b$  was identified as the potential at which the current abruptly increased, and was determined from the intersection of the tangent to the current in the passive range and the rising current in the potential range after breakdown<sup>69,74</sup>. We confirmed in every case that  $E_b$  was truly a breakdown potential, and not a value related to transpassive or uniform corrosion, by reversing the scan direction to negative-going to confirm observation of the expected positive hysteresis.

## 2.3.2. Single-electrode experiments

### 2.3.2.1. Potentiodynamic experiments

The active-passive behaviour of Cu was investigated using the potentiodynamic technique. A ModuLab XM ECS Solartron potentiostat and XM-studio software were used to perform the potentiodynamic experiments. Before each scan, electrodes were prepared as described in section 2.3.1. After 30 min on open circuit to establish a steady  $E_{\text{corr}}$  value, scans were performed as described in section 2.3.1 for multielectrode arrays but with an additional negative-going scan at the same scan rate at the end. The negative-going scan was terminated when the current density became equal to that recorded as the passive current on the positive-going scan.

### 2.3.2.2. Potentiostatic Experiment

Potentiostatic experiments were conducted using a ModuLab XM ECS Solartron potentiostat and XM-studio software. Applied potentials ranging from  $E_{\text{corr}} + 20$  mV to  $E_{\text{corr}} + 105$  mV were selected, based on measured histograms (Section 1.3.1). A second set of potentials, ranging from -27 mV vs SCE to 58 mV vs SCE, was selected to investigate the dependence of passive film morphology and composition on applied potential and charge density. Samples were immersed in the solution immediately after the surface preparation process and a potentiostatic experiment was then performed for 6 hours.

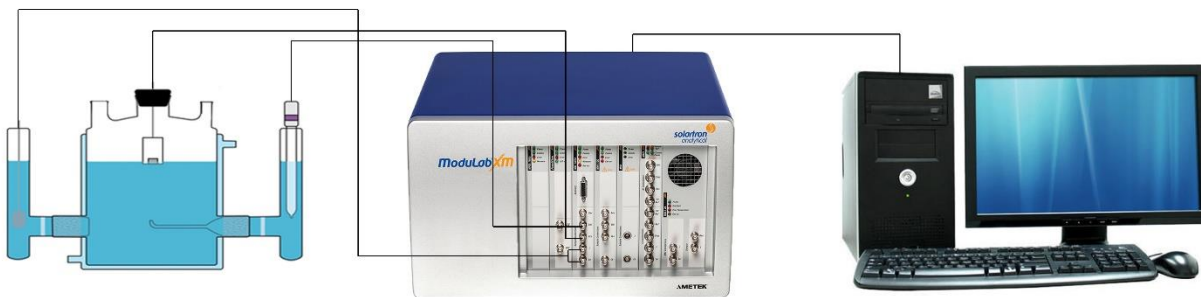


Fig. 4: Schematic of single-electrode cell setup.

## 2.4. Surface analysis

On completion of electrochemical experiments, specimens were rinsed with Type I water, dried in a low stream of Ar gas to avoid damage to oxide films, and stored in an anaerobic chamber until surface analysis could be performed. In some cases, corrosion products were removed by exposing the specimen to an Ar-sparged 9.1 wt%  $\text{HClO}_4$  solution containing 3.5 g/L of  $\text{C}_6\text{H}_{12}\text{N}_4$  as an inhibitor to prevent further Cu corrosion. Scanning electron microscopy

(SEM) and energy dispersive X-ray spectroscopy (EDS) were used to investigate the surface morphology and composition of the film using a Hitachi SU8230 (Regulus Ultra High-Resolution Field Emission SEM) equipped with a FlatQuad EDS (Bruker X-Flash FQ5060 Annular Quad) at Surface Science Western (SSW). A LEO 1540XB SEM equipped with a focused ion beam (FIB) (Zeiss Nano Technology System Division, Germany) at Western Nanofabrication Facility was used to examine the cross-sectional morphology and thickness of oxide films.

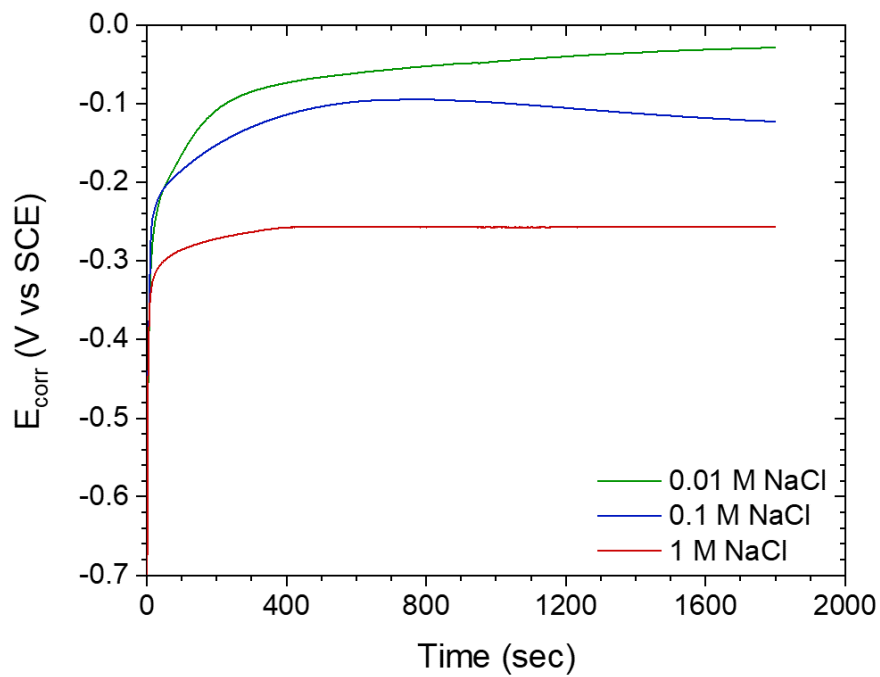
A Kratos AXIS Supra equipped with a monochromatic Al-K $\alpha$  X-ray source (1486.6 eV) was used for X-ray photoelectron spectroscopic analyses. The instrument work function was calibrated to give a binding energy (BE) of 83.96 eV for the Au 4f<sub>7/2</sub> line for metallic Au and the spectrometer dispersion was adjusted to give a BE of 932.62 eV for the Cu 2p<sub>3/2</sub> line of metallic Cu. Survey spectra were recorded over a BE range of 0 to 1200 eV using a pass energy of 160 eV at a step size of 1 eV. High-resolution spectra were collected for the Cu 2p<sub>3/2</sub> and C 1s lines and the CuL<sub>3</sub>M<sub>4,5</sub>M<sub>4,5</sub> Auger peak using a pass energy of 20 eV and a step size of 0.1 eV. In all cases, the Cu 2p<sub>3/2</sub> and Auger LMM lines were collected first to mitigate the effect of X-ray degradation of the Cu(II) state. All spectra were corrected for charging using the adventitious carbon peak (C 1s, 284.8 eV). Data processing was carried out using CasaXPS (v. 2.3.14) software with a Shirley background subtraction. The deconvolution procedures were performed using previously determined fitting parameters <sup>75</sup>.

### 3. Results and Discussion

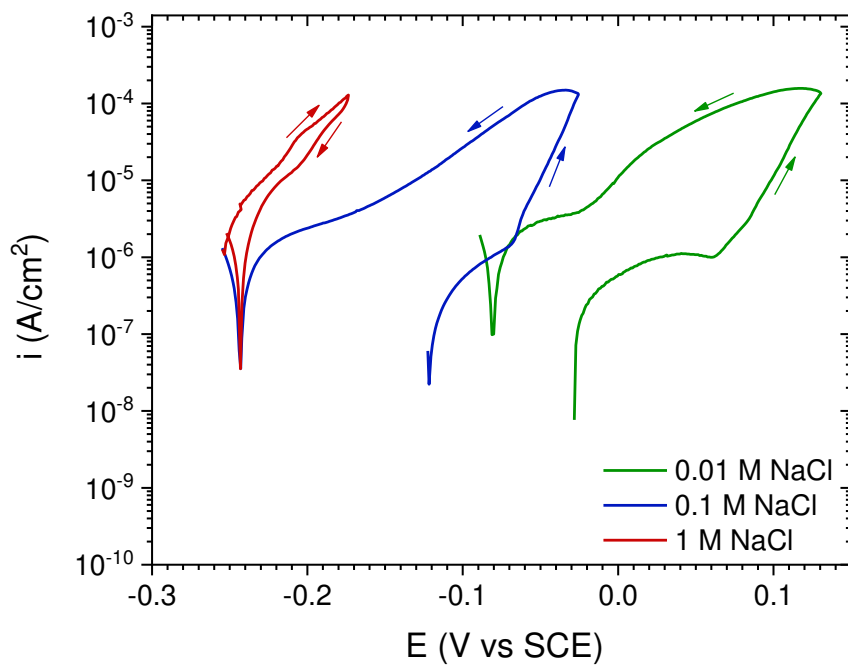
#### 3.1. Potentiodynamic polarization

Fig. 5 shows that E<sub>corr</sub> values, measured in aerated solutions containing different [Cl<sup>-</sup>], increased with time towards a steady-state value which decreased with increasing [Cl<sup>-</sup>]. This decrease with increasing [Cl<sup>-</sup>] can be attributed to acceleration of the anodic dissolution of Cu in Cl<sup>-</sup>-containing solutions, which proceeds via a sequence of electrochemical and chemical steps, as shown in reactions 1 to 3 <sup>76</sup>,





**Fig. 5** Corrosion potential ( $E_{\text{corr}}$ ) of Cu in chloride-containing solutions



**Fig. 6:** Potentiodynamic polarization (PDP) scans recorded on Cu in  $\text{Cl}^-$ -containing solutions.

Fig. 6 shows cyclic polarization scans recorded on Cu in solutions with different  $[Cl^-]$ . In 0.01 M  $Cl^-$ , a passive region is clearly visible on the positive-going scan, followed by film breakdown, indicated by the current increase at more positive potentials. The positive hysteresis observed on the negative-going scan confirmed that the surface was more active on the negative-going scan, most likely due to the initiation of pitting corrosion sites on the negative-going scan. In 0.1 M  $Cl^-$ , the passive region was considerably narrower (Fig. 6), indicating that oxide breakdown was more readily achieved. The large hysteresis shows that repassivation was not readily achieved at this concentration. For 1 M NaCl, the rapid increase in current on the positive-going scan, the absence of a clear passive region, and the maintenance of the current on the negative-going scan indicate active corrosion behaviour. There is a possibility that the rapid dissolution of the  $CuCl$  layer (reaction 1-b), followed by hydrolysis (reaction 4), caused deposition of a marginally protective  $Cu_2O$  film on the surface, resulting in the slight negative hysteresis in the negative-going scan

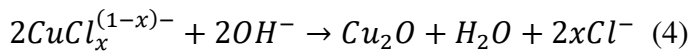
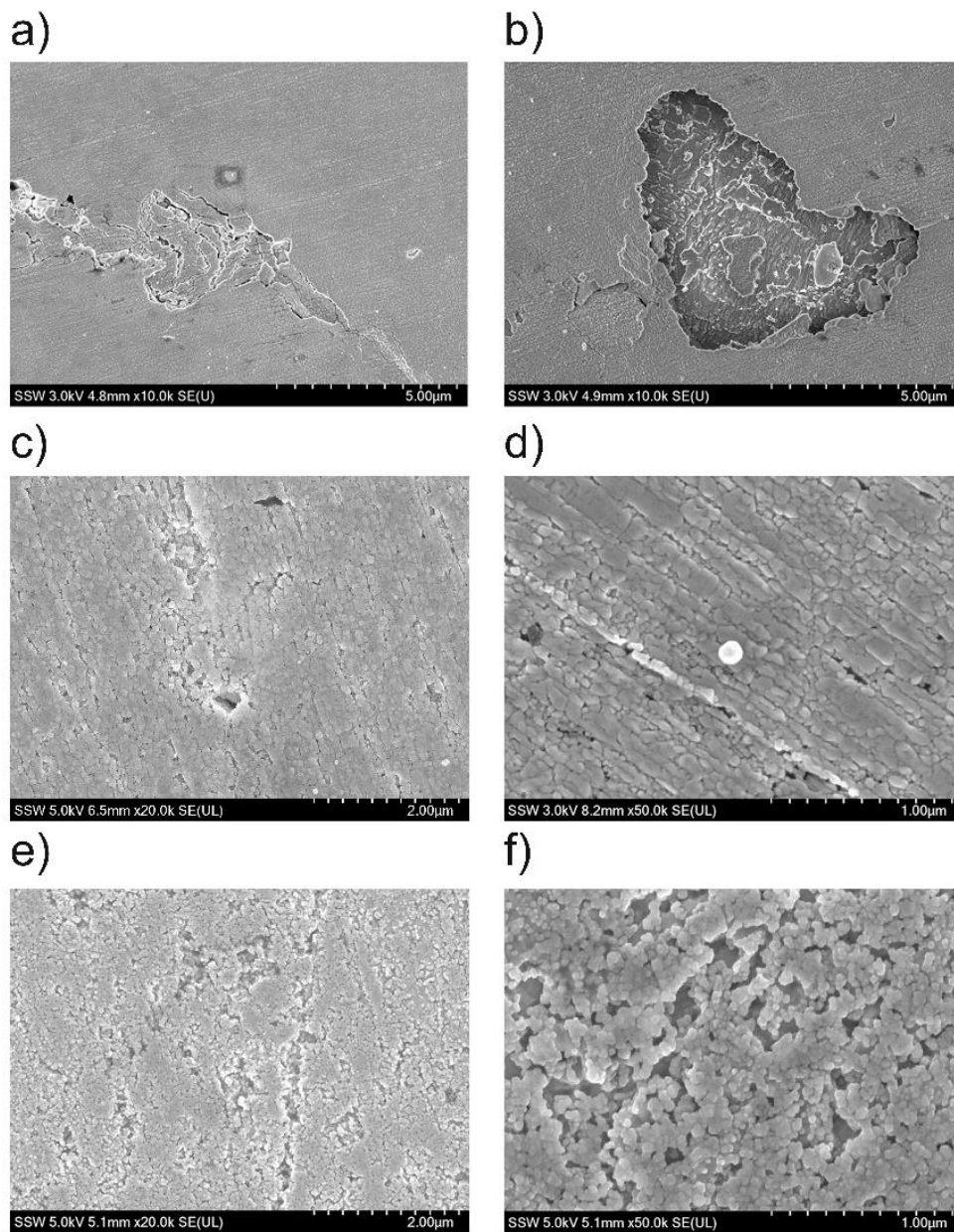


Fig. 7 shows SEM micrographs recorded on Cu surfaces exposed to solutions of different  $[Cl^-]$  (after potentiodynamic polarization experiments). Clear evidence for passive film breakdown was only observed in 0.01 M  $Cl^-$  solution (Fig. 7-a,b). The passive film present after polarization in 0.01 M NaCl solution appears to have been formed by a combination of localized breakdown and transpassive dissolution, since the oxide was electrochemically unstable and could be dissolved simultaneously as the pit tried to propagate, resulting in the formation of shallow pits<sup>27</sup>. A uniform film was observed on Cu in 0.1 M  $Cl^-$ , with the presence of a number of porous sites on the surface (Fig. 7-c,d). In 1 M  $Cl^-$  solution, a generally porous oxide film was observed, with no visible sign of localized attack (Fig. 7-e,f). The porosity of the oxide film could be due to the higher dissolution rate of Cu (via reactions 1 to 3) followed by the formation of  $Cu_2O$  on the Cu surface via reaction 4. The presence of this film could obscure the presence of localized corrosion sites.



**Fig. 7;** Passive film morphology of Cu surfaces after potentiodynamic polarization scans recorded in buffer solutions with different  $[\text{Cl}^-]$ : a,b) 0.01 M  $\text{Cl}^-$  ; c,d) 0.1 M  $\text{Cl}^-$  ; e,f) 1 M  $\text{Cl}^-$  .

### 3.2. Statistical Analysis

Fig. 8 shows sets of  $E_{\text{corr}}$  profiles (a and c) and polarization scans (b and d) recorded at two  $[\text{Cl}^-]$  on a multielectrode array, with the latter showing  $E_b$ . Fig. 9 shows the corresponding histograms and box plots for measured  $E_{\text{corr}}$  and  $E_b$  values. Both  $E_{\text{corr}}$  and  $E_b$  distributions shifted to more negative values with increasing  $[\text{Cl}^-]$ , as expected based on the results in Figures 5 and

6. Also, the difference between  $E_{\text{corr}}$  and  $E_b$  ( $|E_b - E_{\text{corr}}|$ ) decreased with the increase in  $[\text{Cl}^-]$  (Fig. 9a and b). This is consistent with the formation of a more protective film in 0.01 M  $\text{Cl}^-$  under open-circuit conditions, leading to a wider range of  $E_{\text{corr}}$  values compared to those recorded in 0.1 M  $\text{Cl}^-$ . A possible explanation is that more  $\text{Cl}^-$  adsorbed on the oxide films in 0.1 M  $\text{Cl}^-$  promoting breakdown, leading to a shift in  $E_b$  to more negative values, and allowing the enhancement of Cu dissolution (Fig 9b and d).

Less dispersion of  $E_{\text{corr}}$  and  $E_b$  values was observed in solutions containing a higher  $[\text{Cl}^-]$ , Fig. 9a and b. The frequency of breakdown was higher at the higher  $[\text{Cl}^-]$  which created a narrower distribution of  $E_b$  values. At the lower  $[\text{Cl}^-]$ , the passive film was more stable and breakdown required a higher potential, with a decreased frequency of breakdown leading to a wider distribution in  $E_b$  values. The distribution range of  $E_b$  was greater than that for  $E_{\text{corr}}$  in 0.01 M  $\text{Cl}^-$  (Fig. 9a); however, the same distribution range and shape were observed in 0.1 M  $\text{Cl}^-$  for both  $E_{\text{corr}}$  and  $E_b$  (Fig. 9b).

The pitting probability is determined by the statistical distributions of measured values, as defined by the shape parameter and scale factor of the distribution, and the difference between the highest  $E_{\text{corr}}$  and lowest  $E_b$  values. The shape of the distribution of  $E_b$  in 0.01 M  $\text{Cl}^-$  was left-skewed, which might increase the pitting probability of Cu by generating a greater overlap between  $E_{\text{corr}}$  and  $E_b$ . The difference between  $E_b$  and  $E_{\text{corr}}$  ( $E_b^{\text{min}} - E_{\text{corr}}^{\text{max}}$ ) was 74 mV and 51 mV in 0.01 M and 0.1 M  $\text{Cl}^-$  solutions, respectively (Fig. 9a and b); as a result, a greater pitting probability would be expected at the higher  $[\text{Cl}^-]$ . It is important to note that passive behaviour was observed in solutions with  $[\text{Cl}^-]$  up to 0.1 M, followed by active corrosion at higher  $[\text{Cl}^-]$ .

Box plots show the presence of extreme values for both parameters except  $E_{\text{corr}}$  at 0.01 M  $\text{Cl}^-$ , Fig. 9c and d. The pitting probability depends on the overlap between  $E_{\text{corr}}$  and  $E_b$ , so extreme values increase the pitting probability of Cu significantly, specifically when they are located on the left side of the  $E_b$  distribution or the right side of the  $E_{\text{corr}}$  distribution.

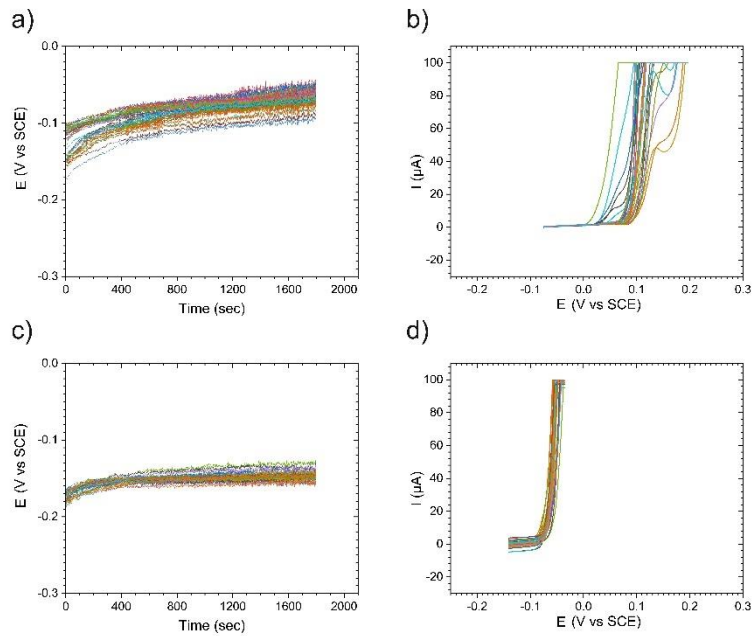


**Fig. 8:** Corrosion potentials ( $E_{\text{corr}}$ ) and polarization curve of Cu multielectrode arrays a,b) 0.01 M  $\text{Cl}^-$  c,d) 0.1 M  $\text{Cl}^-$

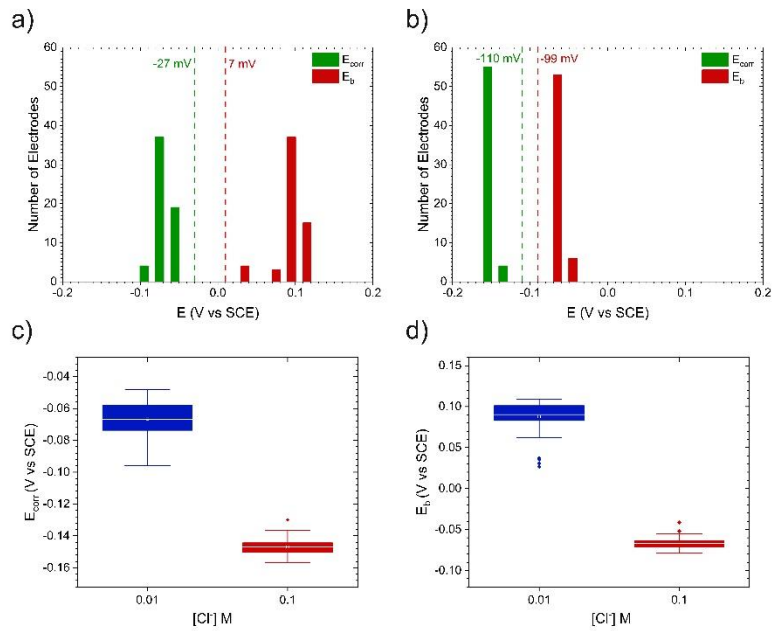


**Fig. 9:** Histograms and box plots for Cu multielectrode arrays; a) histogram of  $E_{\text{corr}}$  and  $E_b$  values in 0.01 M NaCl, b) histogram of  $E_{\text{corr}}$  and  $E_b$  values in 0.1 M NaCl. c) Box plot of  $E_{\text{corr}}$  values in carbonate buffer solutions containing 0.01 and 0.1 M NaCl. d). Box plot of  $E_b$  in carbonate buffer solutions containing 0.01 and 0.1 M NaCl. Green and red dashed lines in Fig. 9a and b define the  $E_{\text{corr}}+20$  mV and  $E_b-20$  mV potentials, respectively. Points in box plots are extreme values.

### 3.3. Potentiostatic polarization

The current-time transients shown in Fig. 10 can be interpreted from two points of view: (I) nucleation and growth of oxide films; (II) initiation and growth of pits.

#### (I) Nucleation and growth of oxide films

Generally, nucleation and growth processes exhibit a current peak attributable to the acceleration of growth of nuclei followed by suppression of growth as the nuclei grow and coalesce to block the surface. In 0.01 M  $\text{Cl}^-$  at an applied potential of -27 mV vs SCE (i.e., 20 mV greater than the maximum  $E_{\text{corr}}$  measured in the multielectrode array experiments), the current-time transient exhibited a sharp decrease (not shown) followed by the establishment of a very low current plateau over the first 21,600 seconds (Fig. 10-b). The current did not exhibit any metastable pitting transients over the full duration of the experiment, indicating the formation of a protective oxide film. At an applied potential of 7 mV vs. SCE (i.e, 20 mV less than the minimum  $E_b$  measured in the multielectrode array experiments), the initial current decreased to a similarly low value but that was followed by an abrupt increase, indicating the breakdown of the initially formed oxide, followed by metal dissolution and the nucleation and growth of oxide and/or hydroxide films. Once the current reached the apex, it decreased at longer times to a lower value approaching a steady-state plateau, indicating the formation of a deposit. The current density did not achieve the extremely low values associated with passivity; this showed that the film was not completely protective, and allowed local dissolution of Cu to continue at a low rate. The initial exponential decay in current over short times (around 70 seconds) suggested film growth via the solid-state mechanism defined by the point defect model (Fig. 10b and d)<sup>12,13,72,77</sup>. The current-time transients were similar to each other in the solution containing 0.1 M  $\text{Cl}^-$  for both applied potentials (defined in Fig. 9), since  $E_b$  was only slightly different to  $E_{\text{corr}}$  (Fig 10-d).

#### (II) Pit growth mechanism

For an applied potential of -27 mV vs. SCE, the current decreased sharply within a short period of time (around 40 seconds) to a value of  $0.6 \mu\text{A}/\text{cm}^2$ , eventually reaching a constant value of  $0.03 \mu\text{A}/\text{cm}^2$ . This extremely low value is consistent with the presence of a passive film. The absence of sharp peaks indicated that there was no metastable pit initiation (Fig. 10-b).

The SEM micrograph of the surface, Fig 11.b, confirms the presence of a thin film with some apparent porosity that suggests there would be a small current observable at longer times.

The current transient recorded at an applied potential close to the lowest  $E_b$  (7 mV vs SCE) exhibited an early sharp decrease, similar to that observed at the lower applied potential of -27 mV vs SCE before breakdown occurred, suggesting the formation of a passive  $Cu_2O$  film prior to breakdown. Subsequently, the current density increased steadily to a maximum after 30 minutes, indicating that film breakdown is a relatively slow, evolving process. The observed current density behaviour suggests that pit growth was under charge transfer control during the early stage as the surface concentration ( $C_{surf}$ ) of dissolved Cu increased, before switching to diffusion control as the current density decreased with time. This could be attributed to an increase in pit depth to a value greater than the critical pit depth ( $r_{sat}$ ), accompanied by corrosion product deposition<sup>52</sup>. The pit growth continued at a very low rate, since the pit was very deep and the deposit was thick (Fig. 11e); therefore, the actual potential at the pit surface was lower than the applied potential, close to  $E_{corr}$ . It is noteworthy that the current did not reach a value indicating passivity. The current density is given by equation (1), in which  $i$  is the current density at the pit surface,  $F$  the faraday constant,  $D_e$  the effective diffusion coefficient, and  $r$  the pit depth.

$$i = 3nFD_eC/2\pi r \quad (1)$$

In a 0.1 M  $Cl^-$  solution, the current density increased to a maximum value after 5,400 and 6,360 seconds at applied potentials of -110 mV and -99 mV vs SCE, respectively. Then the current density decayed to a plateau close to  $0.5 \mu A/cm^2$ , a value lower than that recorded in the 0.01 M NaCl solution. This indicates that pit growth became very slow or even negligible, since this value is close to the expected passive current densities for both -99 mV and -110 mV potentials (Fig 10.d).

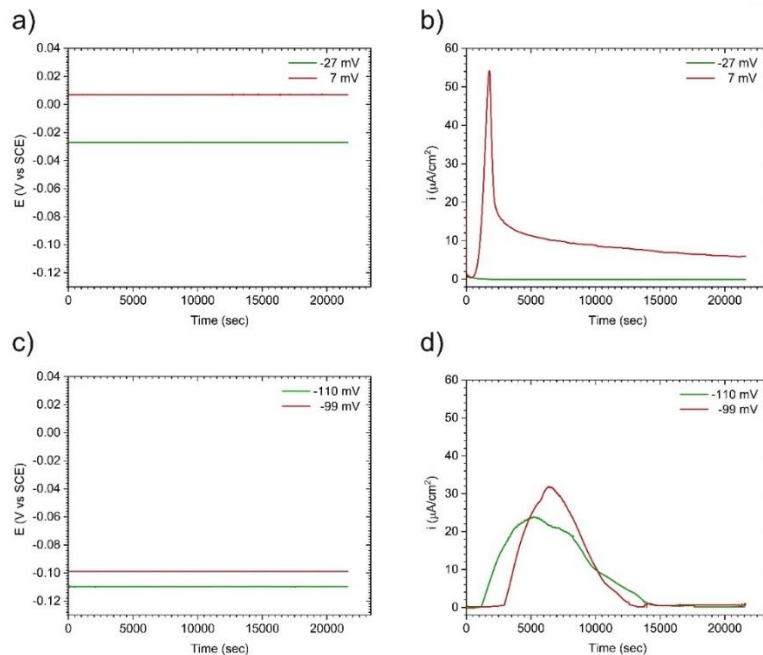
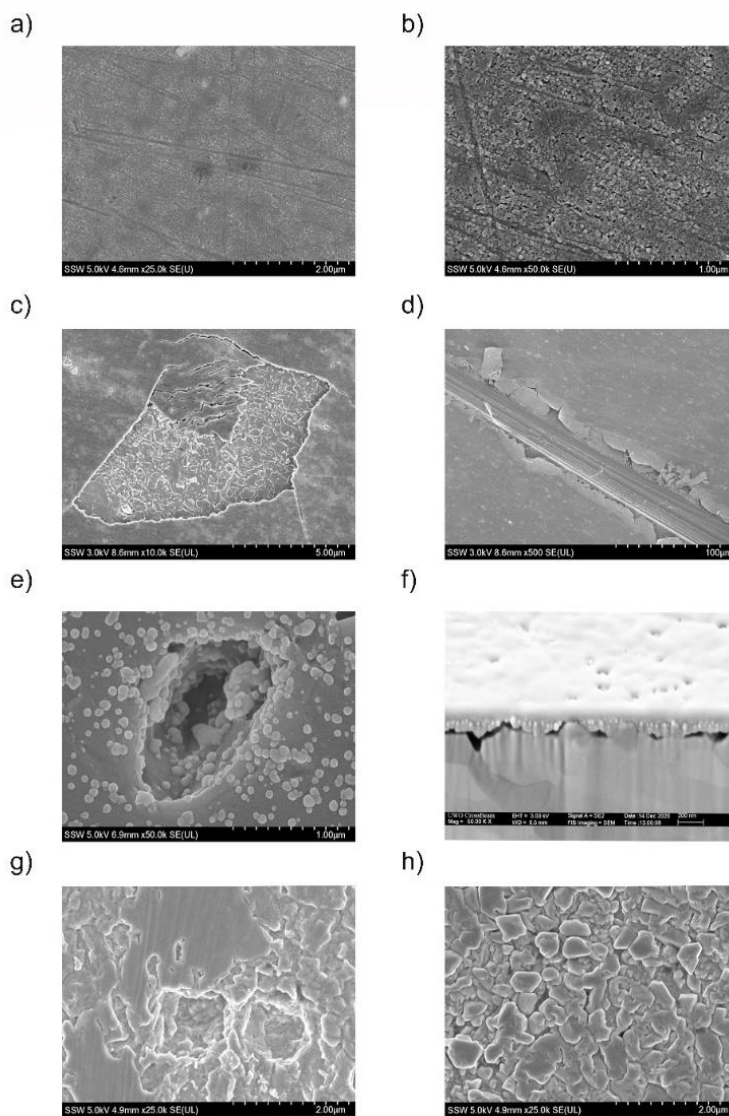


**Fig. 10:** Potential-time and current-time transients recorded on Cu in  $\text{Na}_2\text{CO}_3/\text{NaHCO}_3$  solutions containing different  $[\text{Cl}^-]$ : a) transients at two different applied potentials in  $\text{Na}_2\text{CO}_3/\text{NaHCO}_3$  buffer solution containing 0.01 M NaCl; b) current-time transient in  $\text{Na}_2\text{CO}_3/\text{NaHCO}_3$  buffer solution containing 0.01 M NaCl; c) transients recorded at two different applied potentials in  $\text{Na}_2\text{CO}_3/\text{NaHCO}_3$  buffer solution containing 0.1 M NaCl; d) current-time transient in  $\text{Na}_2\text{CO}_3/\text{NaHCO}_3$  buffer solution containing 0.1 M NaCl.

### 3.4. Surface morphology

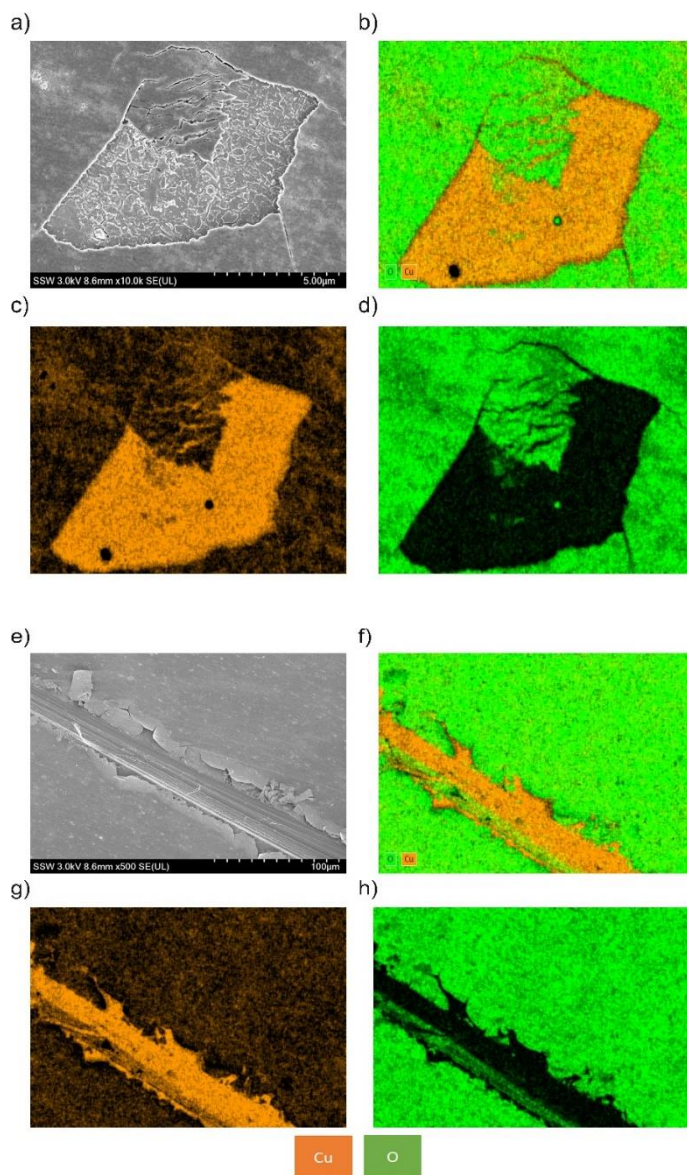
The morphologies of Cu after exposure to 0.01 M  $\text{Cl}^-$  solution at different applied potentials are shown in Fig. 11. After oxidation at -27 mV vs SCE, a thin uniform oxide film covered the surface, with no evidence of any localized attack; no pitting was observed at this applied potential (Fig. 11a and b). At 7 mV vs. SCE, passive film breakdown was observed, as shown in Fig. 11c and d, with the surface deposit formed spalling from the Cu surface most likely after the electrode was removed and dried, as observed in Figure 11-c. Fig. 11-d indicated that such a process could propagate in a longitude direction. A very deep pit with a film at the pit surface was observed, in agreement with a pit growth mechanism achieving diffusion control (Fig. 11-e). Pit initiation and propagation at the intersection of grain boundaries was detected in FIB-cut cross sections (Fig. 11-f). This could be due to the affinity of grain boundaries for adsorbing  $\text{Cl}^-$ , thereby making them preferential locations for localized corrosion<sup>78</sup>.

After removing the passive film from the surface by immersing the Cu sample in an Ar-sparged 9.1 wt% HClO<sub>4</sub> + 3.5 g/L C<sub>6</sub>H<sub>12</sub>N<sub>4</sub> solution, another porous oxide film was observed as an inner layer (Fig. 11-h). The inner oxide film was adhesive and was not removed by immersion of the sample in Ar-sparged 9.1 wt% HClO<sub>4</sub> + 3.5 g/L C<sub>6</sub>H<sub>12</sub>N<sub>4</sub> solution for 5 minutes. Fig. 11-g shows the localized dissolution of Cu leading to the formation of two adjacent pits. Over an extended time period it is possible that the two pits could coalesce into one elongated pit.



**Fig. 11** Surface morphology of Cu in Na<sub>2</sub>CO<sub>3</sub>/ NaHCO<sub>3</sub> buffer solution containing 0.01 M Cl<sup>-</sup>; a,b) oxide film on Cu at the applied potential of -27 mV vs SCE, c-e) oxide film on Cu at the applied potential of 7 mV vs SCE, f) cross-section of the oxide film on Cu at the applied potential of 7 mV vs SCE, g,h) Cu surface at the applied potential of 7 mV vs SCE after the top oxide layer was removed from the surface.

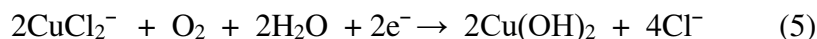
Energy dispersive X-ray analyses (EDX) confirm the exposure of Cu in areas where film rupture has occurred, Figure 12, allowing localized dissolution of Cu in those areas, as seen in Fig. 12b and f.



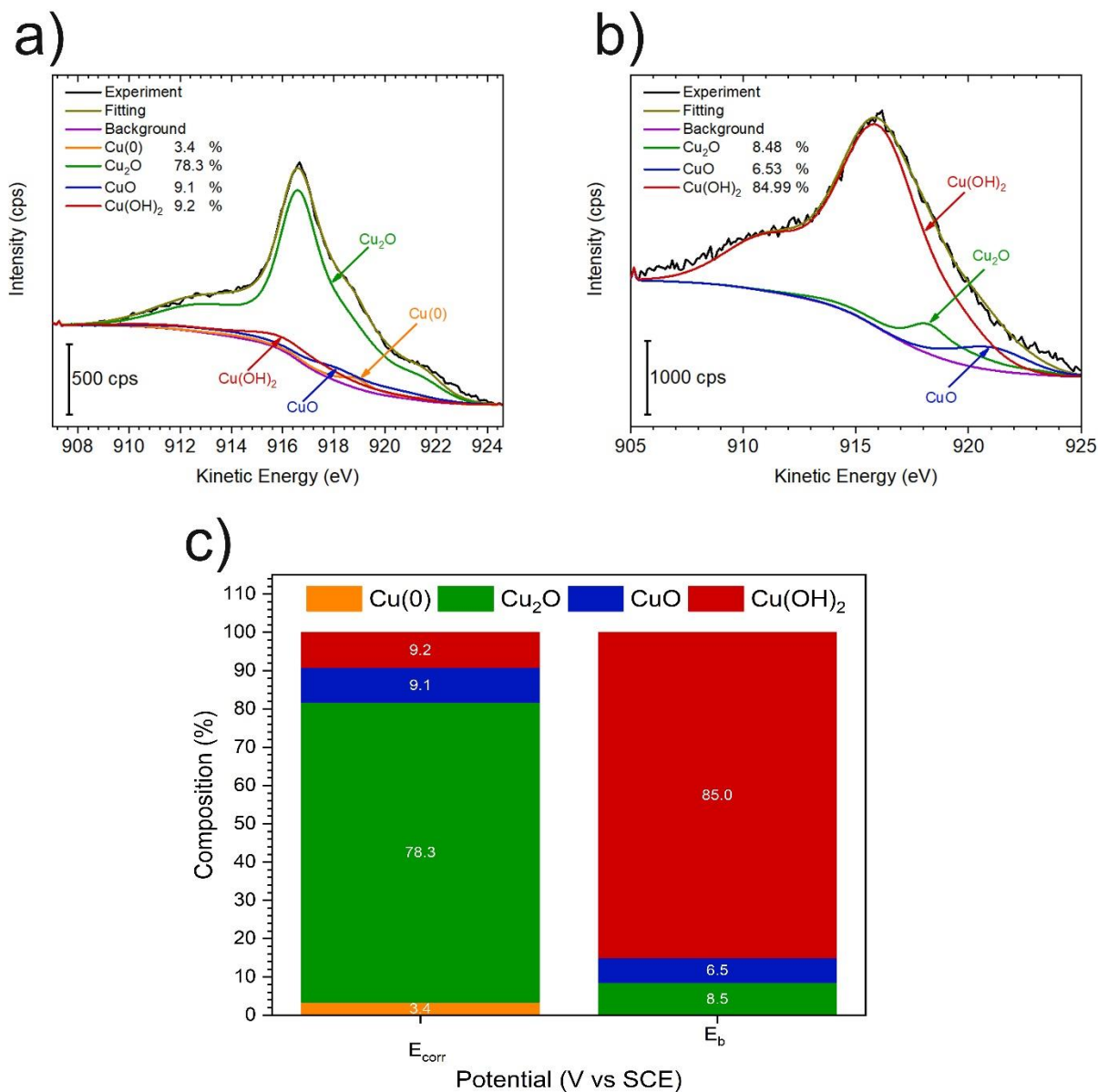
**Fig. 12** EDX map of the passive film on Cu in  $\text{Na}_2\text{CO}_3/\text{NaHCO}_3$  buffer solution containing  $0.01\text{ M Cl}^-$  at an applied potential of  $7\text{ mV vs SCE}$ : a,e) SEM images of passive film breakdown sites; b,f) high-resolution EDX maps of copper and oxygen distributions; c,g) high-resolution EDX maps of copper distribution; d,h) high-resolution EDX maps of oxygen distribution.

Fig. 13 shows the composition of the passive film formed in  $\text{Na}_2\text{CO}_3/\text{NaHCO}_3$  buffer solution containing  $0.01\text{ M NaCl}$  at the applied potentials of  $-27\text{ mV}$  and  $7\text{ mV vs SCE}$ . At a

potential of -27 mV vs SCE (representative of  $E_{\text{corr}}$ ) (Fig 13-a,c), the top surface was dominantly  $\text{Cu}_2\text{O}$ , with small detectable signals for  $\text{CuO}$  and  $\text{Cu}(\text{OH})_2$ . The detection of  $\text{Cu}(0)$  demonstrates that the  $\text{Cu}_2\text{O}$  was present as a thin passive layer, as indicated by the current-time transient in Figure 10b. At the higher applied potential (7 mV vs SCE) the surface was mostly covered with  $\text{Cu}(\text{OH})_2$ , with minimal amounts of  $\text{CuO}$  and  $\text{Cu}_2\text{O}$  detected (Fig. 13-b,c). The hydroxide/oxide film was thick enough that no underlying Cu metal was detectable. The dominance of  $\text{Cu}(\text{OH})_2$  at the higher applied potential (representative of breakdown conditions) can be attributed to a combination of a higher dissolution rate of bare Cu, via the reaction sequence 1a to 1c, and the transpassive oxidation of  $\text{Cu}_2\text{O}$  to  $\text{Cu}^{2+}$ . As dissolved Cu diffused out of the pores in the passive  $\text{Cu}_2\text{O}$  layer, soluble  $\text{Cu}^+$  (as  $\text{CuCl}_2^-$ ) would have been oxidized by soluble  $\text{O}_2$  and the  $\text{Cu}^{2+}$  deposited as  $\text{Cu}(\text{OH})_2$  [25,29]:



Despite the presence of  $\text{HCO}_3^-/\text{CO}_3^{2-}$ ,  $\text{CuCO}_3 \cdot \text{Cu}(\text{OH})_2$  was not deposited, which is in agreement with the observations of Adeloju and coworkers<sup>67</sup>. They claimed that  $\text{HCO}_3^-/\text{CO}_3^{2-}$  stabilized the copper oxide film and did not form another film, (e.g.,  $\text{CuCO}_3 \cdot \text{Cu}(\text{OH})_2$ ) on the surface. As the carbonate concentration increased, its adsorption stabilized the oxide film by preventing  $\text{Cl}^-$  adsorption. It was claimed that the minimum required concentration of  $\text{HCO}_3^-/\text{CO}_3^{2-}$  required for this effect to dominate was equal to or greater than 0.005 M. Nishakata<sup>79</sup> claimed that the presence of carbonate hindered the formation of  $\text{Cu}(\text{OH})_2$ ; however, our results demonstrated the presence of  $\text{Cu}(\text{OH})_2$  under both conditions. In addition, the absence of a peak at  $\sim 289.3$  eV ( $\pm 0.6$  eV) in the C1s spectrum confirmed the absence of surface carbonate species. As a result, we can propose that the formation and amount of  $\text{Cu}(\text{OH})_2$  was not dependent on  $\text{HCO}_3^-/\text{CO}_3^{2-}$  but on the potential.



**Fig. 13** CuL<sub>3</sub>M<sub>4,5</sub>M<sub>4,5</sub> Auger spectra recorded after oxidation in a HCO<sub>3</sub><sup>-</sup>/CO<sub>3</sub><sup>2-</sup> solution containing 0.01 M Cl<sup>-</sup>; a) at -27mV (representative of  $E_{corr}$ ), the surface is mostly covered with Cu(0) and Cu<sub>2</sub>O, b) at -7mV (after film breakdown ( $E_b$ )), surface is mostly covered with Cu(II) oxide and hydroxide with the absence of Cu(0), c) normalized relative film compositions (At%).

The form of the current-time transient at the applied potential of 7 mV vs SCE was consistent with the formation of a Cu(OH)<sub>2</sub> outer layer, Fig. 10b. The current density increase can be attributed to increased exposure of the dissolving Cu surface as breakdown progressed, with the current density peak occurring once deposition of Cu(OH)<sub>2</sub> overwhelmed the dissolution, leading

to a decrease in current density. At pH 9, the solubility of  $\text{Cu}^{2+}$  is very low<sup>80</sup> and local saturation readily achieved. The leveling off of the current density at a moderate value shows the deposited  $\text{Cu}(\text{OH})_2$  to be porous. The partial detachment of the initially formed  $\text{Cu}_2\text{O}$  is consistent with the combination of metal dissolution and transpassive dissolution ( $\text{Cu}_2\text{O} \rightarrow \text{Cu}^{2+}$ ) occurring simultaneously. While pitting was expected, due to the breakdown of the initially formed  $\text{Cu}_2\text{O}$  layer, it was likely to have been obscured by the dissolution-deposition process.

Fig. 14 shows the morphology of Cu surfaces after applying potentials of  $-110$  mV and  $-99$  mV vs SCE in a solution containing  $0.1$  M  $\text{Cl}^-$ . At the lower potential, the surface was covered by a deposited film with a particle size of  $\sim 0.3$  to  $\sim 0.5$   $\mu\text{m}$ , with some areas exhibiting minor porosity. This porosity runs linearly and diagonally across the surface shown in Figure 14a. At higher magnification, Figure 14b reveals small areas where the deposited oxide film appears to have been detached, most likely after removal of the specimen from solution. Other areas experienced shallow pitting and were covered by a thickened deposit with a porous centre, Figure 14d.

At the higher potentials, similar detachment of the surface deposit was observed, exposing visible preferential attack of the metal surface at triple points, Figure 14g. Also, as shown in Figure 14h, corrosion tended to spread across the surface in some areas. Removal of the surface films while avoiding further Cu corrosion revealed both deep pitted locations, Figure 14j, and elongated channels, Figure 14i. It can be noted that the elongated corrosion morphology may reflect the expectation that corrosion could be enhanced in areas covered by porous deposits, as shown in Figure 14a.

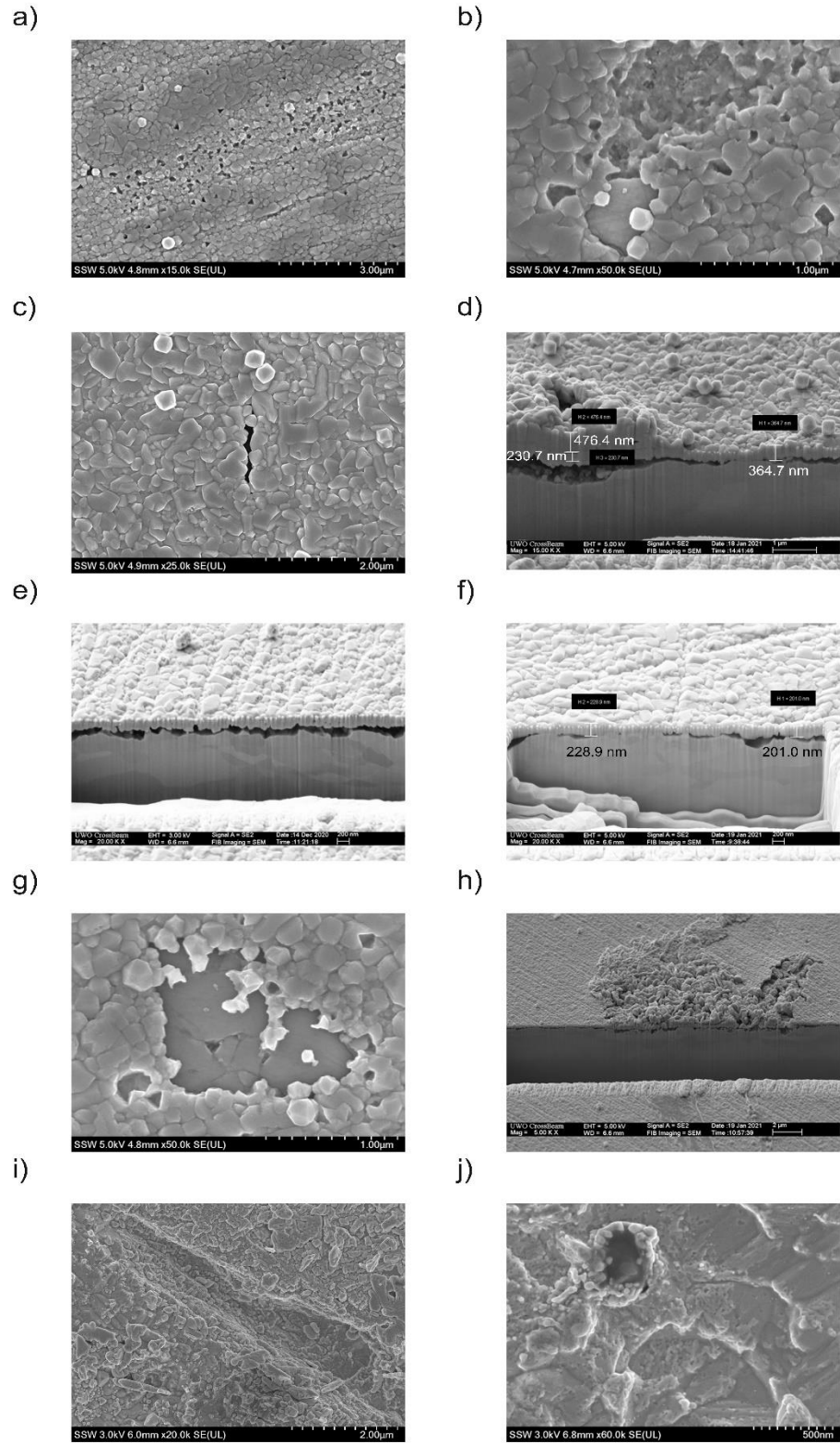


**Fig. 14** Surface morphology of Cu exposed to buffer solutions with 0.1 M  $\text{Cl}^-$  at certain potentials: a-d)  $E_{corr}$ ; e-h)  $E_b$ , before film removal; i,j)  $E_b$ , after film removal.

Figure 15 shows the composition of oxide films formed in 0.1 M NaCl solution at the two different applied potentials as determined by Auger electron spectroscopy. The oxide film was composed of  $\text{Cu}_2\text{O}$  and  $\text{Cu}(\text{OH})_2$ , without any detectable amount of  $\text{CuO}$ .

The O 1s spectrum (not shown here) was analyzed to confirm the presence of hydroxide on the Cu sample after exposure at an applied potential of  $E_b$ . XPS results showed that the uniformly distributed film (Fig. 14 e and f) was a very compact deposit of  $\text{Cu}_2\text{O}$ . Since Cu is more likely to dissolve as  $\text{CuCl}_x^{(1-x)-}$  and the film was dominantly  $\text{Cu}_2\text{O}$ , this would suggest that the deposit was formed predominantly via reaction 2. This observation is in good agreement with the current-time transient (Fig. 10d) which shows an initial period of passivity followed by breakdown. Following the breakdown, there was a large, slow current transient, followed by the re-establishment of a very low current, consistent with a coherent protective film, as shown in Fig. 14 e and f. Several sites experienced obvious shallow pitting, as presented in Fig. 14d, followed by the accumulation of a thicker deposit, which appears to be porous at the center. The pits were not backfilled with corrosion product deposits. A probability would be the formation of  $\text{CuCl}_x^{(1-x)-}$  in the presence of a substantial  $[\text{Cl}^-]$ . Since this reaction consumes  $\text{OH}^-$ , it would decrease the pH locally, which could disturb buffering by  $\text{HCO}_3^-/\text{CO}_3^{2-}$  and inhibit  $\text{Cu}^{2+}$  formation within the pore by increasing its solubility. Beyond the pore, this pH suppression would be neutralized and  $\text{Cu}_2\text{O}$  formation promoted, which could account for the thicker deposit at this location.

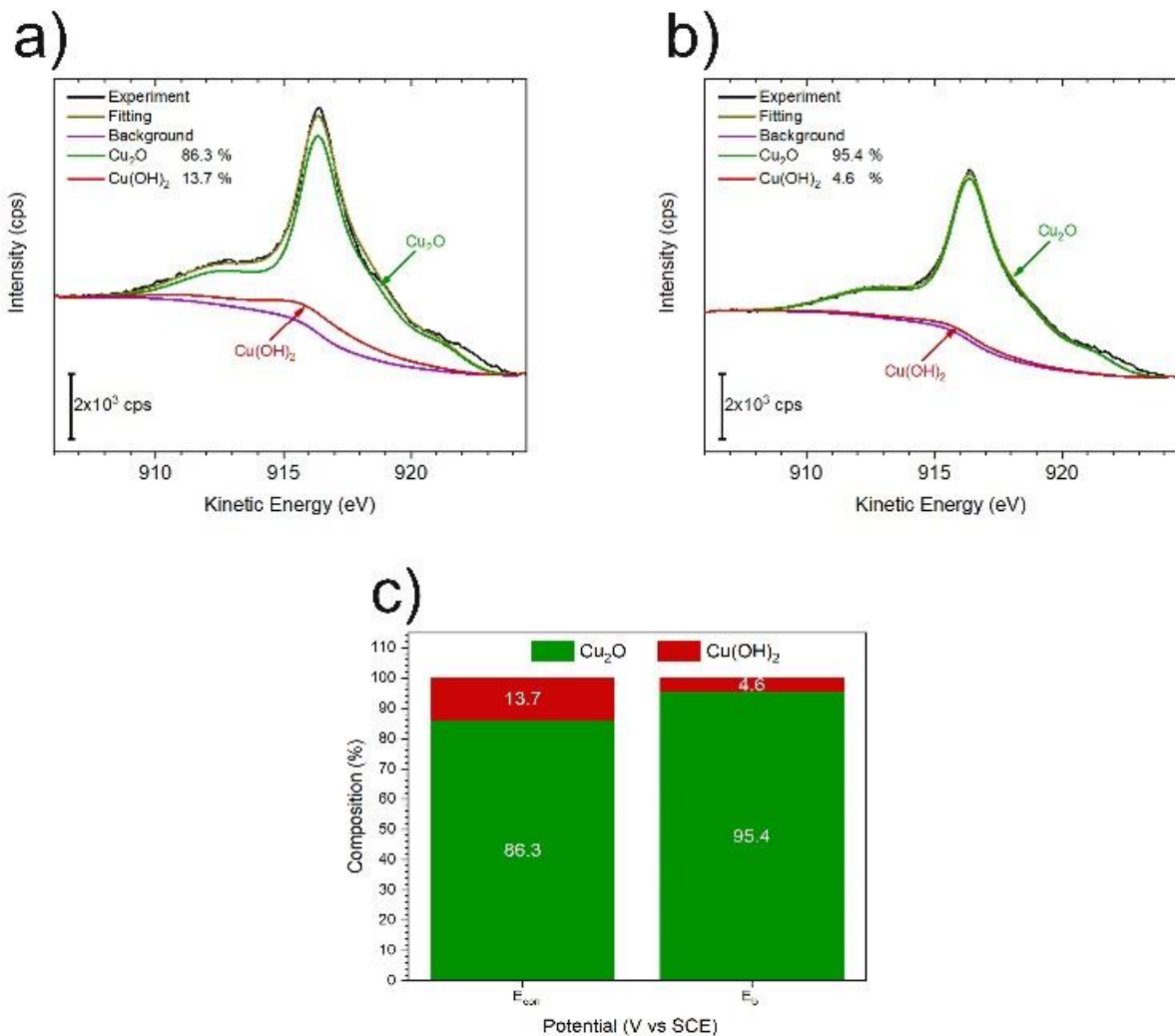


**Fig. 15**  $CuL_3M_{4,5}M_{4,5}$  Auger spectra recorded after oxidation in a  $HCO_3^-/CO_3^{2-}$  solution containing 0.1 M  $Cl^-$  at various potentials: a) -110 mV (representative of  $E_{corr}$ ); b) -99mV (representative of film breakdown,  $E_b$ ); c) normalized relative film compositions (at%) at  $E_{corr}$  and  $E_b$ .

Fig. 16 shows the compositions determined from Auger spectra for two different  $[Cl^-]$  and four different applied potentials. Increasing chloride concentration to 0.1 M hindered the formation of  $CuO$ . Another important point was the dependency of  $Cu_2O$  and  $Cu(OH)_2$  on applied potential, since the surface was mostly covered with  $Cu_2O$  at potentials lower than -27 mV vs SCE; however,  $Cu_2O$  was converted to  $Cu(OH)_2$  with further increases of potential to 7 mV vs SCE.

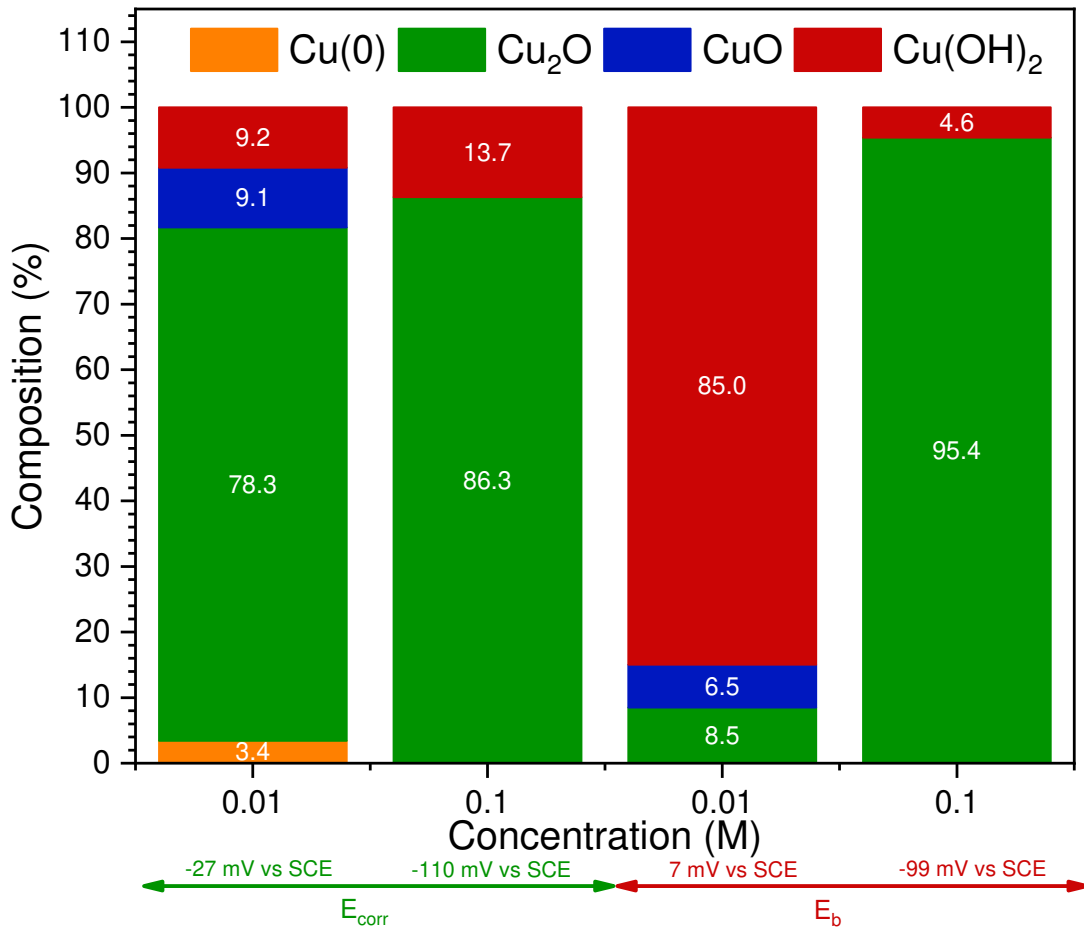


**Fig. 16** Composition of the passive film on Cu in buffer solutions with different  $[Cl^-]$  as determined by Auger electron spectroscopy.

Generally speaking the surface compositions were dominated by either  $Cu_2O$  or  $Cu(OH)_2$ , as shown in Fig. 16. The amounts of  $CuO$  were minimal, making this phase of marginal importance. When the Cu was anodically oxidized at  $-27\text{ mV}$  (in  $0.01\text{ M } Cl^-$ ), when only a low current was observed,  $Cu_2O$  was dominantly formed as a passive layer. When the  $[Cl^-]$  was maintained at  $0.01\text{ M}$  and the potential increased from  $-27\text{ mV}$  to  $+7\text{ mV}$ ,  $Cu(OH)_2$  dominated on the surface; although it was most likely that a sublayer of  $Cu_2O$  persisted but was difficult to detect by XPS. The current density behaviour (Fig 10) confirmed that a short period of passivation, attributable to the formation of  $Cu_2O$ , existed prior to breakdown and an increase in current density, followed by a subsequent decrease in current density, was attributable to the deposition of  $Cu(OH)_2$ . There are three possible mechanisms of formation of the  $Cu^{2+}$  (to form  $Cu(OH)_2$ ):

- I. Reaction of  $\text{CuCl}_2^-$  with dissolved  $\text{O}_2$ ;
- II. Direct metal dissolution as  $\text{Cu}^{2+}$ ;
- III. Conversion of  $\text{Cu}_2\text{O}$  to  $\text{Cu}^{2+}$ .

Reactions II and III are likely for the reasons noted below and because the applied potential in this case (7mV vs SCE) is the most positive of the four potentials investigated.

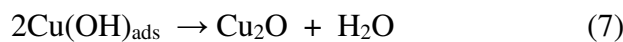
When the  $[\text{Cl}^-]$  was increased to 0.1 M, the potentials applied were considerably lower (-110mV and -99mV vs SCE). In both cases  $\text{Cu}_2\text{O}$  was dominant, with only minimal amounts of  $\text{Cu}(\text{OH})_2$  formed. This could be attributable to the inhibiting effect of  $\text{Cl}^-$  on the reaction of  $\text{CuCl}_2^-$  with  $\text{O}_2$  (to yield  $\text{Cu}^{2+}$ ) as shown by Sharma and Millero<sup>81</sup>. This study showed that the rate decreased by many orders of magnitude as  $[\text{Cl}^-]$  was increased). At the lower  $[\text{Cl}^-]$ ,  $\text{Cu}^{2+}$  formation occurred (leading to  $\text{Cu}(\text{OH})_2$  deposition), suggesting that it could be formed by the reaction of  $\text{CuCl}_2^-$  with dissolved  $\text{O}_2$ . These observations indicate that the dominant influence on the behaviour was potential. If breakdown did not occur until the specimen was polarized to a positive potential at which the direct ( $\text{Cu} \rightarrow \text{Cu}^{2+}$ ;  $\text{Cu}_2\text{O} \rightarrow \text{Cu}^{2+}$ ) and indirect ( $\text{Cu}^+ + \text{O}_2 \rightarrow \text{Cu}^{2+}$ ) reactions were dominant,  $\text{Cu}(\text{OH})_2$  deposition dominated, yielding only partial passivation.

A combination of  $\text{Cl}^-$  and high potential is supported by the differences in the initial current density behaviour on first applying the potential. The initial passive period is short at high potentials (7 mV) but extended at lower potentials (-110 mV and -99 mV). Other features to be explained are the longer current density transients at low potential and high  $[\text{Cl}^-]$  and the observation that the film eventually formed at the lower potentials (-110 mV and -99 mV) and higher  $[\text{Cl}^-]$  is considerably more protective, despite a protracted period of high current density. This indicates that, despite film breakdown, extensive dissolution, and the possibility of pitting, redeposition of  $\text{Cu}_2\text{O}$  eventually blocks the surface. Three mechanisms are possible<sup>76</sup>:

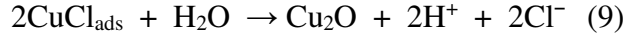
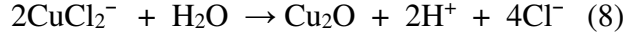
I. The combination of



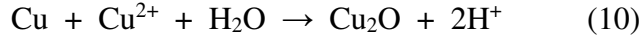
and



II. Hydrolysis of  $\text{CuCl}_2^-$



III. Conversion to  $\text{Cu}^{2+}$  does occur to some extent (by reaction with  $\text{O}_2$ ), followed by the reaction:



Since the  $\text{Cu}_2\text{O}$  is formed compactly on the surface (i.e., the current density is strongly suppressed), all reactions except reaction 8 seem possible, although we were not able to separate them with current results.

### 3.5. Effect of applied potential on the pitting probability of Cu

Different applied potentials were selected within the highest range of  $E_{\text{corr}}$  and extreme values of  $E_b$  to investigate the pitting susceptibility of Cu in bicarbonate buffer solutions containing 0.01 M  $\text{Cl}^-$  at pH 9 (Fig. 17).

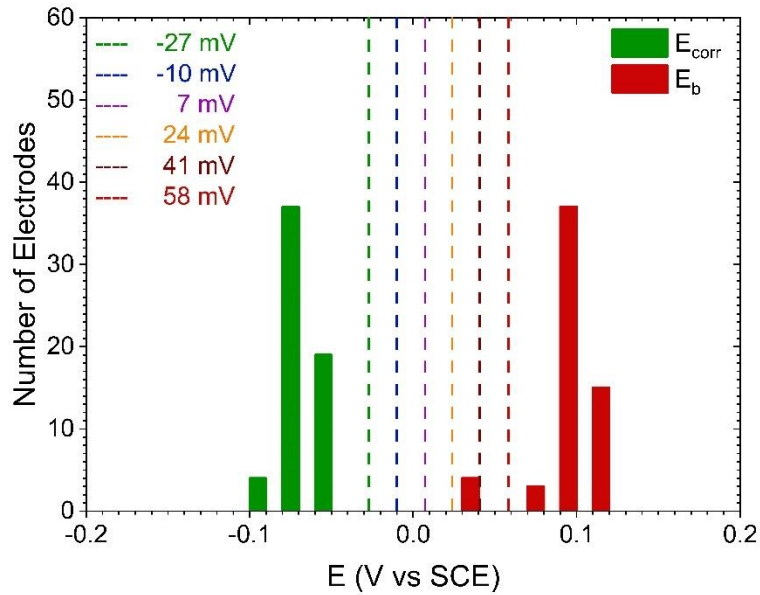


**Fig. 17** Range of applied potentials in bicarbonate buffer solutions containing 0.01 M  $\text{Cl}^-$  based on the histograms of  $E_{\text{corr}}$  and  $E_b$  values.

Fig. 18-a shows the current-time transients at different applied potentials. The peak current density changed slightly from -10 mV to 24 mV; however, the peak current density increased significantly with further increase of the applied potential to 41 mV (greater charge density) (Fig.

18-d,e). The time of pit initiation is the time at which the current begins to increase. Since only passive film formation occurred at the lowest potential (-27 mV vs SCE), this can be considered as establishing a baseline for the other current-time transients. Although a considerably larger charge was consumed at the two highest applied potentials, the current recorded at longer times only increased slightly as the potential was increased. This suggested that the overall reactivity of the surface was not particularly dependent on potential; i.e., the  $\text{Cu}(\text{OH})_2$  film became protective except for the residual breakdown sites.

Pitting was observed for potentials greater than -10 mV vs SCE (Fig. 18-a). Increasing the potential to 41 mV caused a longitudinal breakdown of the passive films, leading to the pitting corrosion of Cu along the breakdown sites. Also, a covered pit was observed (Fig 19-i). Based on the LSF framework<sup>40-42,51,52</sup>, the pit interior could be either smooth or crystallographic, depending on the perforation size ( $a$ ) of the covered pit. The pit is under diffusion control if  $a < a_{\text{sat}}$  and under charge transfer control when  $a_{\text{sat}} < a < a_{\text{crit}}$ . However, we did not remove the oxide film to investigate the morphology of the underlying pit and the size of the perforation. As shown in Fig. 19-k through n, at an applied potential of 58 mV, a large portion of the passive film was dissolved, and this exposed the bare Cu to the aggressive solution. Shoesmith et al.<sup>12</sup> proposed the same anodic charge and oxide film morphology for different applied potentials when the potential was equal to or greater than -220 mV, suggesting that passive film morphology was independent of potential and a charge dependent phenomena; however, our result indicated an increase of charge density with potential (Fig. 18-d). Also, the oxide film morphology was determined to be a potential-dependent parameter.

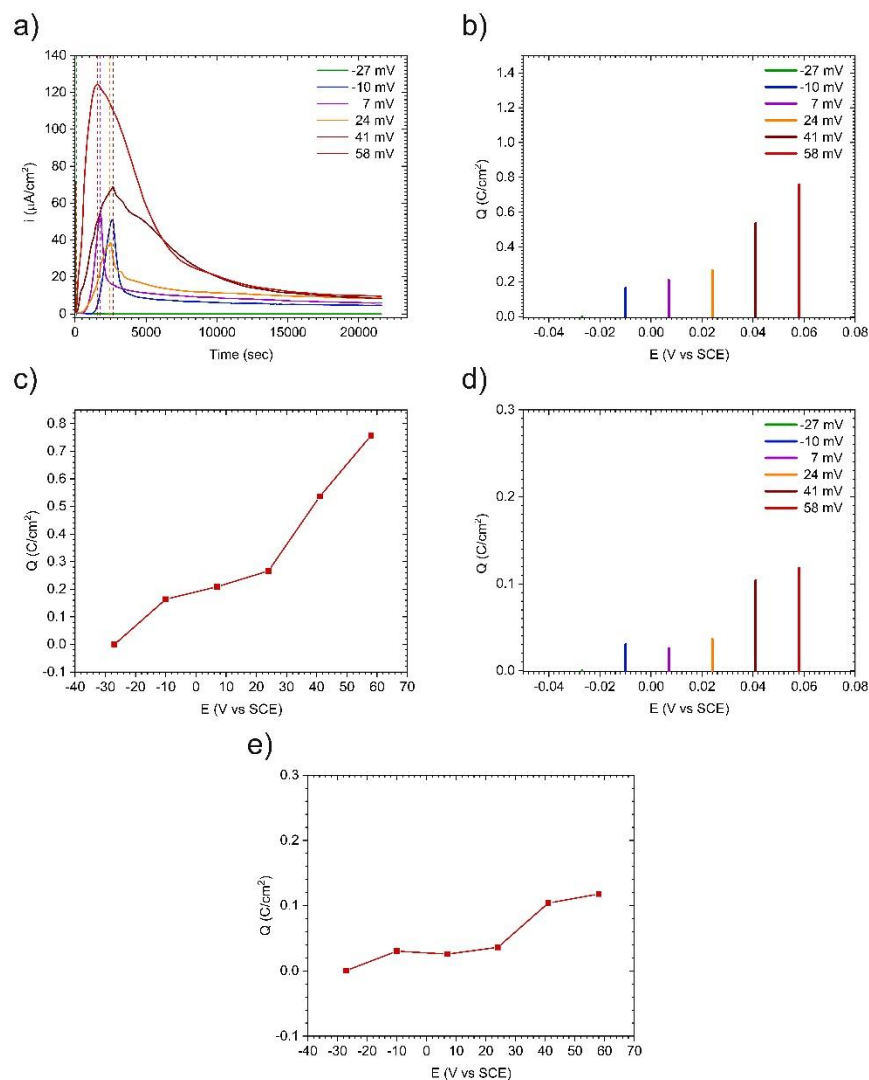


**Fig. 18** a) Current-time transients at different applied potentials b,c) Cumulative charge density at different applied potentials d,e) Cumulative charge density (peak current) at different applied potentials.

Different pitting morphologies have been observed, depending on the applied potential (Fig. 19-a through j). At lower applied potentials, the passive film was almost intact and only a few small pits were observed on the surface (Fig. 19-a to d). Increasing the applied potential to 7 mV resulted in breakdown of the passive film. Also, hemispherical pits were observed, with the presence of chloride at the pit surface (Fig. 19-e). The pitting morphology was different at 41 and 58 mV since the pits propagated longitudinally. This could be the result of pit propagation along the grain boundaries. Also, a large amount of the passive film was completely dissolved at these applied potentials and a large frequency of covered pits was observed at higher applied potentials

(Fig. 19-i through n). It is noteworthy to mention that corrosion product deposits grew perpendicular to the passive film, which might result in the mechanical breakdown of the passive film (Fig. 19-h,k). Increasing the applied potential contributed to the dissolution of a large area of the passive film, as observed in Fig. 19-k. EDX results (Fig. 20) indicated the presence of copper chloride species ( $\text{CuCl}$  or  $\text{CuCl}_2$ ) on the Cu surface where the passive film was ruptured. These could eventually oxidize to  $\text{Cu}^{2+}$ , yielding  $\text{Cu}(\text{OH})_2$ , as shown in the XPS results (Fig. 21). Also, formation of  $\text{Cu}_2\text{O}$  via reaction 2 appears not to have been the dominant reaction, based on the XPS results (Fig. 21). Our results indicate extensive and severe damage (pitting corrosion) at higher potentials; more dissolution of the oxide film and higher susceptibility to breakdown have been observed in samples with higher charge densities.

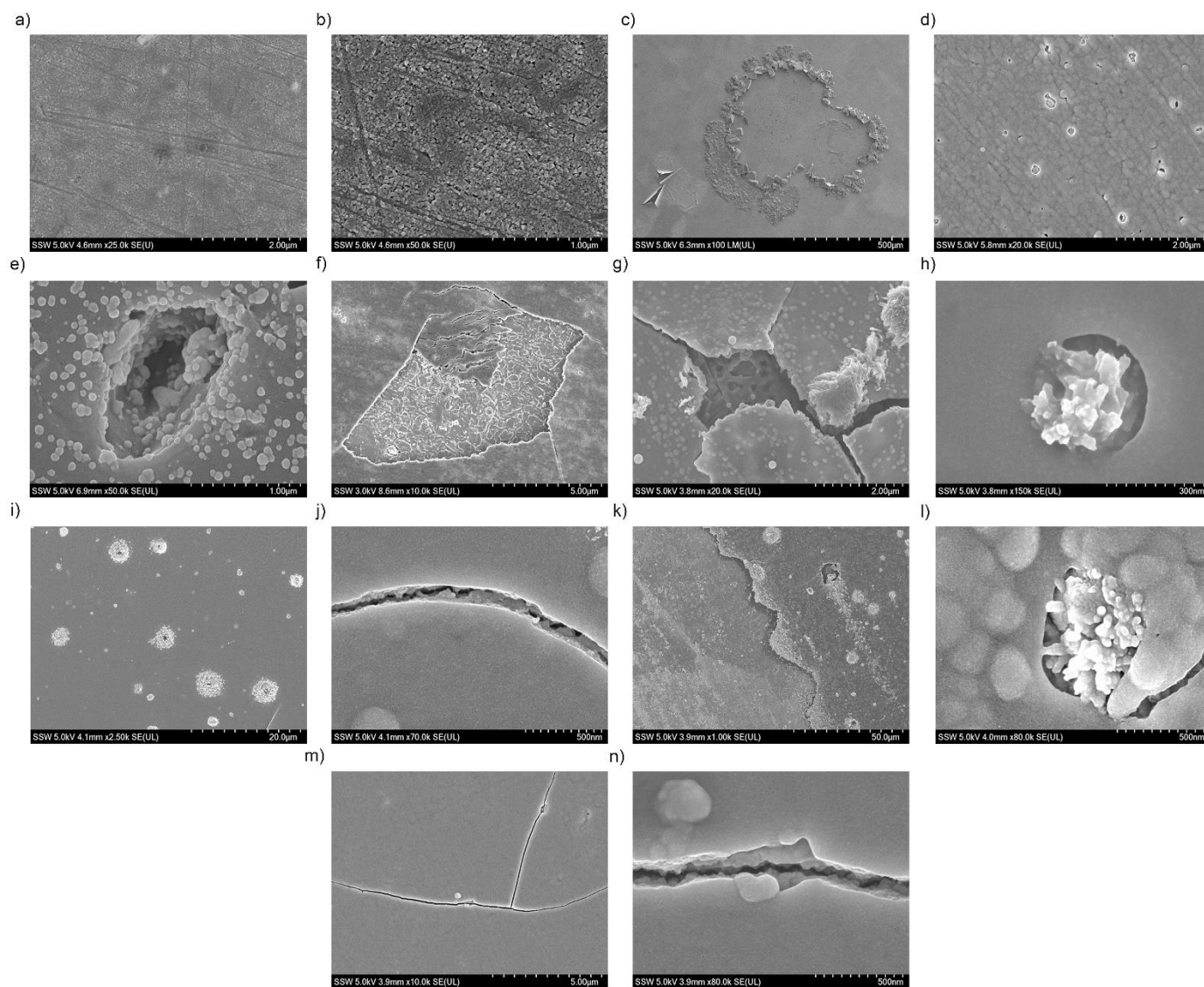


**Fig. 19** Surface morphology of Cu in buffer solutions with 0.01 M  $\text{Cl}^-$  and different applied potentials: a,b) -27 mV; c,d) -10 mV; e,f) 7 mV; g,h) 24 mV; i,j) 41 mV; k,l,m,n) 58 mV.

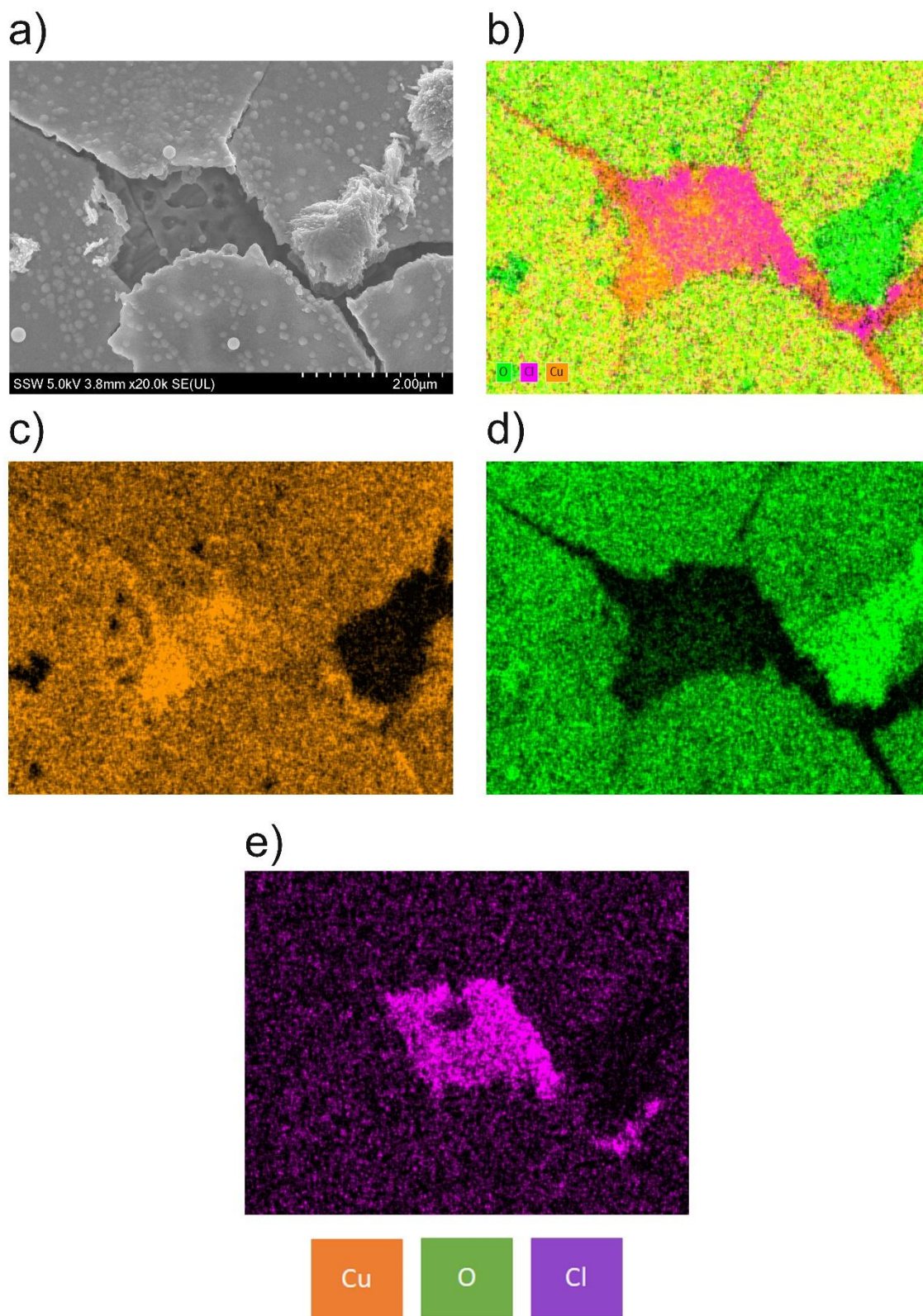
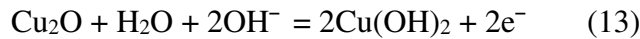
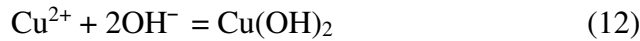


**Fig. 20** EDX map of passive film after exposure to buffer solution with 0.01 M  $\text{Cl}^-$  at an applied potential of 24 mV vs. SCE.

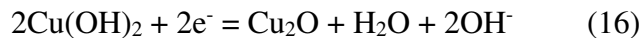
The compositions of oxide films are shown in Fig. 21. A small amount of Cu(0) is observed only at a potential of -27 mV (close to  $E_{\text{corr}}$ ), while the surface is mostly covered with a passive film of  $\text{Cu}_2\text{O}$ . The minimal amounts of  $\text{CuO}/\text{Cu}(\text{OH})_2$  may reflect a minor reactivity. Even though the film had not broken down, it clearly shows what looks like some chemical attack that could have led to  $\text{Cu}(\text{OH})_2$  formation. The surface was covered, mostly with  $\text{Cu}(\text{OH})_2$ , by a further increase of applied potential, which occurred either directly from base Cu or/and from the conversion of  $\text{Cu}_2\text{O}$  and  $\text{CuO}$  through the reactions 11 to 14. In this case, Cu(0) was undetectable



The greatest amount of  $\text{Cu}(\text{OH})_2$  was observed at 7 mV (close to the lowest  $E_b$ ) and then the percentage of  $\text{Cu}(\text{OH})_2$  decreased and the amount of  $\text{CuO}$  increased with further increase of applied potential, probably due to the conversion of  $\text{Cu}(\text{OH})_2$  to  $\text{CuO}$  via reaction 15:



Moreover, the amount of  $\text{Cu}_2\text{O}$  increased with further increases in applied potential, due to the reduction of  $\text{Cu}(\text{OH})_2$  to  $\text{Cu}_2\text{O}$  via reaction 16:



As shown in Fig. 21, XPS results indicate that increasing the potential from -27 mV to 7 mV resulted in the conversion of Cu(0) and  $\text{Cu}_2\text{O}$  to  $\text{Cu}(\text{OH})_2$ , while the amount of  $\text{CuO}$  changed slightly. For potentials greater than 7 mV, two possible conversions could happen depending on the range of applied potential. The  $\text{Cu}(\text{OH})_2$  was converted to  $\text{CuO}$  and  $\text{Cu}_2\text{O}$  with increasing the potential from 7 mV to 24 mV, and then a further increase of the applied potential to 41 mV resulted in the conversion of  $\text{Cu}_2\text{O}$  to  $\text{CuO}$  and  $\text{Cu}(\text{OH})_2$ . Finally, the amount of  $\text{Cu}(\text{OH})_2$  decreased while  $\text{CuO}$  and  $\text{Cu}_2\text{O}$  increased with increasing of the potential to 58 mV. It is important to note that the amount of  $\text{CuO}$  increased with applied potential, but  $\text{Cu}(\text{OH})_2$  and  $\text{Cu}_2\text{O}$  either increased or decreased with increases in the applied potential. As a result, no clear

relationship was observed between the composition of the film and the applied potential. One reason could be that XPS only shows the composition of the top 5-8 nm of the surface, so it does not convey the fractional composition of the total film.

Shoosmith et al.<sup>12</sup> claimed that passive film morphology was independent of applied potential but a charge-dependent phenomenon; however, our XPS and electrochemical results indicated the dependency of passive film morphology on both the potential and the charge density. At lower applied potentials, the rate of metal dissolution and supersaturation is low at the metal surface, so the surface will be mostly covered by  $\text{Cu}_2\text{O}$ . On the other hand, the dissolution rate increases with further increases in the applied potential, leading to the minimum required supersaturation condition on the metal surface. In this case, the surface will be covered mostly with  $\text{CuO}$  or/and  $\text{Cu}(\text{OH})_2$ .

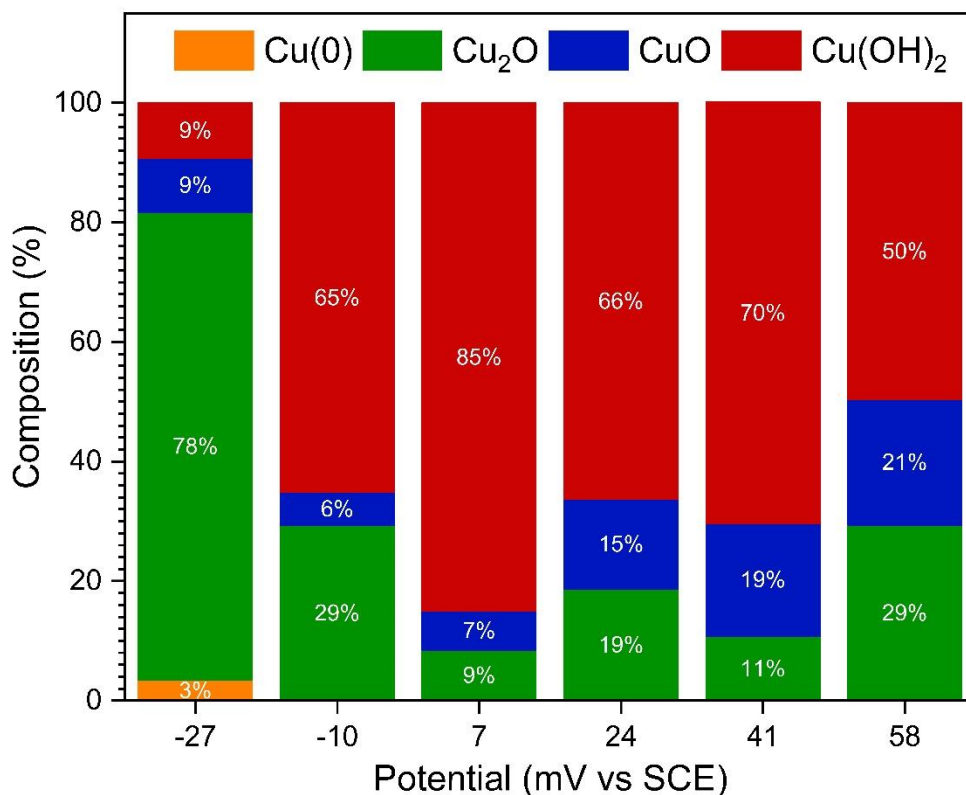


**Fig. 21** Compositions of passive films grown at different applied potentials in buffer solution with 0.01 M  $\text{Cl}^-$ .

#### 4. Conclusions

A series of potentiodynamic and potentiostatic experiments were conducted in bicarbonate buffer solutions with different chloride concentrations to study the pitting susceptibility and passive film morphology of Cu. The surface compositions of samples were examined using the XPS technique to create a solid understanding of the effect of applied potential and charge density on the morphology and composition of the passive film.  $E_{\text{corr}}$  shifted to more negative values at higher  $[\text{Cl}^-]$  due to the greater rate of dissolution. SEM images of specimens after potentiodynamic experiments showed a large passive film breakdown at lower  $[\text{Cl}^-]$  while uniform corrosion was observed at higher  $[\text{Cl}^-]$ . The frequency of breakdown increased with  $[\text{Cl}^-]$  resulting in a narrower distribution of  $E_b$ . The pitting probability of Cu increased with increasing  $[\text{Cl}^-]$  due to the lower difference between  $E_{\text{corr}}$  and  $E_b$  ( $E_{\text{corr}} - E_b$ ) in 0.1 M  $\text{Cl}^-$  solution. In 0.01 M  $\text{Cl}^-$  solution, no pitting was observed when the applied potential was close to  $E_{\text{corr}}$ ; however, deep pits were observed when the applied potential was chosen to be close to  $E_b$  (7 mV vs SCE). Increasing the  $[\text{Cl}^-]$  resulted in initiation and propagation of pits even at potentials close to  $E_{\text{corr}}$ , which was in good agreement with our statistical analysis. XPS analysis indicated a mixed oxide layer composed of  $\text{Cu}_2\text{O}$ ,  $\text{CuO}$ , and  $\text{Cu}(\text{OH})_2$ .  $\text{Cu}(0)$  was only observed on specimens that were exposed to 0.01 M  $\text{Cl}^-$  solution at potentials close to  $E_{\text{corr}}$ , due to the formation of a porous and non-protective film on the Cu surface. The composition of the passive film was dependent on both the  $[\text{Cl}^-]$  and the applied potential. Both the passive film morphology and the charge density were dependent on the applied potential, so different breakdown mechanisms and passive film compositions were determined at the different applied potentials.

#### Acknowledgment:

This research was jointly funded by the Natural Sciences and Engineering Research Council of Canada, and the Nuclear Waste Management Organization through Alliance Grant ALLRP561193-20. Assistance provided by personnel at University Machine Services and Western Nanofabrication Facility is gratefully acknowledged.

## References:

- 1 Newman, R. C. 2001 W.R. Whitney award lecture-Understanding the corrosion of stainless steel. *Corrosion* **57**, 1030-1041 (2001).
- 2 Salinas-Bravo, V. M. & Newman, R. C. An alternative method to determine critical pitting temperature of stainless steels in ferric chloride solution. *Corrosion Science* **36**, 66-77 (1994).
- 3 Gaudet, G. T. *et al.* Mass transfer and electrochemical kinetic interactions in localized pitting corrosion. *AIChE Journal* **32**, 949-958 (1986).
- 4 Laycock, N. J., Moayed, M. H. & Newman, R. C. Metastable pitting and the critical pitting temperature. *Journal of The Electrochemical Society* **145**, 2622-2628 (1998).
- 5 Pistorius, P. C. & Burstein, G. T. Metastable pitting corrosion of stainless steel and the transition to stability. *Royal Society London* **341**, 531-559 (1992).
- 6 Pride, S. T., Scully, J. R. & Hudson, J. L. Metastable pitting of aluminum and criteria for the transition to stable pit growth. *Journal of The Electrochemical Society* **141**, 3028-3040 (1994).
- 7 Frankel, G. S., Stockert, L., Hunkeler, F. & Boehni, H. Metastable pitting of stainless steel. *Corrosion* **43**, 429-436 (1987).
- 8 Frankel, G. S. Pitting corrosion of metals: A review of the critical factors. *Journal of The Electrochemical Society* **145**, 2186-2198 (1998).
- 9 Galvele, J. R. Transport processes and the mechanism of pitting of metals. *Journal of The Electrochemical Society* **123**, 464-474 (1976).
- 10 Frankel, G. S. & Sridhar, N. Understanding localized corrosion. *Materials Today* **11**, 38-44, doi:10.1016/s1369-7021(08)70206-2 (2008).
- 11 Miller, B. Split-Ring disk study of the anodic processes at a copper electrode in alkaline solution. *Journal of Electrochemical Society* **116** (1969).
- 12 Shoesmith, D. W., Rummery, T. E., Owen, D. & Lee, W. Anodic oxidation of copper in alkaline solutions I. Nucleation and growth of cupric hydroxide films. *Journal of The Electrochemical Society* **123**, 790-799 (1976).
- 13 Milosev, I., Metikos-Hukovic, M., Drogowska, M. & Menard, H. Breakdown of passive film on copper in bicarbonate solutions containing sulfate ions. *Journal of The Electrochemical Society* **139**, 2409-2418 (1992).
- 14 Ambrose, J., Barradas, R. G. & Shoesmith, D. W. Investigation of copper in aqueous alkaline solutions by cycling voltammetry. *Journal of Electroanalytical Chemistry and Interfacial Electrochemistry* **47**, 47-64 (1973).
- 15 Ashworth, V. & Fairhurst, D. The anodic formation of Cu<sub>2</sub>O in alkaline solutions. *Journal of The Electrochemical Society* **124**, 506-517 (1977).
- 16 Drogowska, M., Brossard, L. & Menard, H. Comparative study of copper behaviour in bicarbonate and phosphate aqueous solutions and effect of chloride ions. *Journal of Applied Electrochemistry* **24** (1994).
- 17 Chialvo, M. R. G. d., Zerbino, J. O. & Marchiano, S. L. Correlation of electrochemical and ellipsometric data in relation to the kinetics and mechanism of Cu<sub>2</sub>O electroformation in alkaline solutions. *Journal of Applied Electrochemistry* **16**, 517-526 (1986).
- 18 Adeloju, S. B. & Hughes, H. C. The corrosion of copper pipes in high chloride-low carbonate mains water. *Corrosion Science* **26**, 851-870 (1986).
- 19 Chialvo, M. R. G. d. & Arvia, A. J. The electrochemical behaviour of copper in alkaline solutions containing sodium sulphide. *Journal of Applied Electrochemistry* **15**, 685-696 (1985).
- 20 Park, C. J., Lohrengel, M. M., Hamelmann, T., Pilaski, M. & Kwon, H. S. Grain-dependent passivation of surfaces of polycrystalline zinc. *Electrochimica Acta* **47**, 3395-3399 (2002).

- 21 Kunze, J., Maurice, V., Klein, L. H., Strehblow, H.-H. & Marcus, P. In situ STM study of the duplex passive films formed on Cu(111) and Cu(001) in 0.1 M NaOH. *Corrosion Science* **46**, 245-264, doi:10.1016/s0010-938x(03)00140-9 (2004).
- 22 Chialvo, M. R. G. D., Salvarezza, R. C., Moll, D. V. & Arvia, A. J. Kinetics of passivation and pitting corrosion of polycrystalline copper in borate buffer solutions containing sodium chloride. *Electrochimica Acta* **30**, 1501–1511 (1985).
- 23 Lill, K. A., Hassel, A. W., Frommeyer, G. & Stratmann, M. Scanning droplet cell investigations on single grains of a FeAlCr light weight ferritic steel. *Electrochimica Acta* **51**, 978-983, doi:10.1016/j.electacta.2005.05.068 (2005).
- 24 Martinez-Lombardia, E. *et al.* Scanning electrochemical microscopy to study the effect of crystallographic orientation on the electrochemical activity of pure copper. *Electrochimica Acta* **116**, 89-96, doi:10.1016/j.electacta.2013.11.048 (2014).
- 25 Naseer, A. & Khan, A. Y. A study of growth and breakdown of passive film on copper surface by electrochemical impedance spectroscopy. *Turkish Journal of Chemistry* **33**, 739 - 750, doi:10.3906/kim-0708-23 (2009).
- 26 Al-Kharafi, F. M. & El-Tantawy, Y. A. Passivation of copper: Role of some anions in the mechanism of film formation and breakdown. *Corrosion Science* **22**, 1-12 (1982).
- 27 Ambrose, J., Barradas, R. G. & Shoesmith, D. W. Rotating copper disk electrode studies of the mechanism of the dissolution-passivation step on copper in alkaline solutions. *Journal of Electroanalytical Chemistry and Interfacial Electrochemistry* **47**, 65-80 (1973).
- 28 Speckmann, H. D., Lohrengel, M. M., Schultze, J. W. & Strehblow, H. H. The growth and reduction of duplex oxide films on copper. *Ber. Bunsenges. Phys. Chem* **89**, 392-402 (1985).
- 29 Cong, H. & Scully, J. R. Use of coupled multielectrode arrays to elucidate the pH dependence of copper pitting in potable water. *Journal of The Electrochemical Society* **157**, 36 - 46, doi:10.1149/1.3251288 (2010).
- 30 McIntyre, N. S., Sunder, S., Shoesmith, D. W. & Stanchell, F. W. Chemical information from XPS—applications to the analysis of electrode surfaces. *Journal of Vacuum Science and Technology* **18**, 714-721, doi:10.1116/1.570934 (1981).
- 31 Allah, A. G. G., Abou-Romia, M. M., Badawy, W. A. & Rehan, H. H. Effect of halide ions on passivation and pitting corrosion of copper in alkaline solutions. *Materials and Corrosion* **42**, 584-591 (1991).
- 32 Strehblow, H. H. & Titze, B. The investigation of the passive behaviour of copper in weakly acid and alkaline solutions and the examination of the passive film by ESCA and ISS. *Electrochimica Acta* **25**, 839-850 (1980).
- 33 Kolics, A., Polkinghorne, J. C. & Wieckowski, A. Adsorption of sulfate and chloride ions on aluminum.pdf. *Electrochimica Acta* **43**, 2605-2618 (1998).
- 34 Yu, S. Y., O'Grady, W. E., Ramaker, D. E. & Natishan, P. M. Chloride ingress into aluminum prior to pitting corrosion-an investigation by XANES and XPS. *Journal of Electrochemical Society* **147** (2000).
- 35 Natishan, P. M. & O'Grady, W. E. Chloride ion interactions with oxide-covered aluminum leading to pitting corrosion: A Review. *Journal of The Electrochemical Society* **161**, C421-C432, doi:10.1149/2.1011409jes (2014).
- 36 Li, T., Liu, L., Zhang, B., Li, Y. & Wang, F. Growth of single corrosion pit in sputtered nanocrystalline stainless steel film. *Corrosion Science* **111**, 186-198, doi:10.1016/j.corsci.2016.05.007 (2016).
- 37 Laycock, N. J. & Newman, R. C. Localised dissolution kinetics, salt films and pitting potentials. *Corrosion Science* **39**, 1771-1790 (1997).

- 38 Marcus, P., Maurice, V. & Strehblow, H. H. Localized corrosion (pitting): A model of passivity breakdown including the role of the oxide layer nanostructure. *Corrosion Science* **50**, 2698-2704, doi:10.1016/j.corsci.2008.06.047 (2008).
- 39 Frankel, G. S., Li, T. & Scully, J. R. Localized corrosion: Passive film breakdown vs pit growth stability. *Journal of The Electrochemical Society* **164**, C180-C181, doi:10.1149/2.1381704jes (2017).
- 40 Li, T., Scully, J. R. & Frankel, G. S. Localized corrosion: passive film breakdown vs pit growth stability: part II. A model for critical pitting temperature. *Journal of The Electrochemical Society* **165**, C484-C491, doi:10.1149/2.0591809jes (2018).
- 41 Li, T., Scully, J. R. & Frankel, G. S. Localized Corrosion: Passive Film Breakdown vs. Pit Growth Stability: Part III. A Unifying Set of Principal Parameters and Criteria for Pit Stabilization and Salt Film Formation. *Journal of The Electrochemical Society* **165**, C762-C770, doi:10.1149/2.0251811jes (2018).
- 42 Li, T., Scully, J. R. & Frankel, G. S. Localized corrosion: passive film breakdown vs. pit growth stability: part IV. The role of salt film in pit growth: A mathematical framework. *Journal of The Electrochemical Society* **166**, C115-C124, doi:10.1149/2.0211906jes (2019).
- 43 Kong, D. C. *et al.* Long-term polarisation and immersion for copper corrosion in high-level nuclear waste environment. *Materials and Corrosion* **68**, 1070-1079, doi:10.1002/maco.201609415 (2017).
- 44 Srinivasan, J. & Kelly, R. G. One-dimensional pit experiments and modeling to determine critical factors for pit stability and repassivation. *Journal of The Electrochemical Society* **163**, C759-C767, doi:10.1149/2.0651613jes (2016).
- 45 Maurice, V., Yang, W. P. & Marcus, P. X-ray photoelectron spectroscopy and scanning tunneling microscopy study of passive films formed on (100) Fe-18Cr-13Ni single-crystal surfaces. *Journal of The Electrochemical Society* **145**, 909-920 (1998).
- 46 Maurice, V., Yang, W. P. & Marcus, P. XPS and STM investigation of the passive film formed on Cr(110) single-crystal surfaces. *Journal of The Electrochemical Society* **141**, 3016-3027 (1994).
- 47 Sato, N. A theory for breakdown of anodic oxide films on metals. *Electrochimica Acta* **16**, 1683-1692 (1971).
- 48 Wei, X. *et al.* Electrochemical measurements and atomistic simulations of Cl<sup>-</sup>-induced passivity breakdown on a Cu<sub>2</sub>O film. *Corrosion Science* **136**, 119-128, doi:10.1016/j.corsci.2018.02.057 (2018).
- 49 Huang, R., Horton, D. J., Bocher, F. & Scully, J. R. Localized corrosion resistance of Fe-Cr-Mo-W-B-C bulk metallic glasses containing Mn+Si or Y in neutral and acidified chloride solution. *Corrosion* **66** (2010).
- 50 Silverman, D. C. *Practical corrosion prediction using electrochemical techniques*. (John Wiley & Sons, Inc., 2011).
- 51 Li, T., Wu, J. & Frankel, G. S. Localized corrosion: Passive film breakdown vs. Pit growth stability, Part VI: Pit dissolution kinetics of different alloys and a model for pitting and repassivation potentials. *Corrosion Science* **182**, doi:10.1016/j.corsci.2021.109277 (2021).
- 52 Li, T., Scully, J. R. & Frankel, G. S. Localized corrosion: passive film breakdown vs pit growth stability: part V. Validation of a new framework for pit growth stability using one-dimensional artificial pit electrodes. *Journal of The Electrochemical Society* **166**, C3341-C3354, doi:10.1149/2.0431911jes (2019).
- 53 Souto, R. M., Gonzalez, S., Salvarezza, R. C. & Arvia, A. J. Kinetics of copper passivation and pitting corrosion in Na<sub>2</sub>SO<sub>4</sub> containing dilute NaOH aqueous solution. *Electrochimica Acta* **39**, 2619-2628 (1994).

- 54 Cong, H., Michels, H. T. & Scully, J. R. Passivity and pit stability behavior of copper as a function of selected water chemistry variables. *Journal of The Electrochemical Society* **156**, 16-27 (2009).
- 55 Ruijini, G., Srivastava, S. C. & Ives, M. B. Pitting corrosion behavior of UNS N08904 stainless steel in a chloride-sulfate solution. *Corrosion* **45** (1989).
- 56 Sridhar, N. & Cragnolino, G. A. Applicability of Repassivation Potential for Long-Term Prediction of Localized Corrosion of Alloy 825 and Type 316L Stainless Steel. *Corrosion* **49**, 885-894 (1993).
- 57 Woldemedhin, M. T., Srinivasan, J. & Kelly, R. G. Effects of environmental factors on key kinetic parameters relevant to pitting corrosion. *Journal of Solid State Electrochemistry* **19**, 3449-3461, doi:10.1007/s10008-015-2816-9 (2015).
- 58 Srinivasan, J., Liu, C. & Kelly, R. G. Geometric Evolution of Flux from a Corroding One-Dimensional Pit and Its Implications on the Evaluation of Kinetic Parameters for Pit Stability. *Journal of The Electrochemical Society* **163**, C694-C703, doi:10.1149/2.1221610jes (2016).
- 59 Dunn, D. S., Sridhar, N. & Cragnolino, G. A. Long-Term prediction of localized corrosion of alloy 825 in high-level nuclear waste repository environments. *Corrosion* **52**, 115-124 (1996).
- 60 Srinivasan, J. & Kelly, R. G. On a recent quantitative framework examining the critical factors for localized corrosion and its impact on the Galvele pit stability criterion. *Corrosion* **73**, 613-633 (2017).
- 61 Laycock, N. J. & Newman, R. C. Temperature dependence of pitting potentials for austenitic stainless steels above their critical pitting temperature. *Corrosion Science* **40**, 887-902 (1998).
- 62 Leckie, H. P. & Uhlig, H. H. Environmental factors affecting the critical potential for pitting in 18-8 stainless steel. *Journal of The Electrochemical Society* **113**, 1262-1267 (1966).
- 63 King, F., Quinn, M. J. & Litke, C. D. Oxygen reduction on copper in neutral NaCl solution. *Journal of The Electrochemical Society* **385**, 45-55 (1995).
- 64 Mayanna, S. M. & Setty, T. H. V. Role of chloride ions in relation to copper corrosion and inhibition. *Proceedings of the Indian Academy of Sciences - Section A* **80**, 184-193 (1974).
- 65 Kong, D. *et al.* Effect of chloride concentration on passive film properties on copper. *Corrosion Engineering, Science and Technology* **53**, 122-130, doi:10.1080/1478422x.2017.1413160 (2017).
- 66 Kong, D. *et al.* Size matching effect between anion vacancies and halide ions in passive film breakdown on copper. *Electrochimica Acta* **292**, 817-827, doi:10.1016/j.electacta.2018.10.004 (2018).
- 67 Adeloju, S. B. & Duan, Y. Y. Influence of bicarbonate ions on stability of copper oxides and copper pitting corrosion. *British Corrosion Journal* **29**, 315-320, doi:10.1179/000705994798267520 (1994).
- 68 Smart, N. G. & Bockris, J. O. M. Effect of Water Activity on Corrosion. *Corrosion* **48**, 277-280 (1992).
- 69 Mankowski, G., Duthil, J. P. & Giusti, A. The pit morphology on copper in chloride- and sulphate-containing solutions. *Corrosion Science* **39**, 27-42 (1997).
- 70 Venu, K., Balakrishnan, K. & Rajagopalan, K. S. A potentiokinetic polarization study of the behaviour of steel in NaOH-NaCl system. *Corrosion Science* **5**, 59-69 (1965).
- 71 Alvarez, M. G. & Galvele, J. R. Pitting of high purity Zinc and pitting potential significance. *Corrosion* **32**, 284-294 (1976).
- 72 Macdonald, D. The point defect model for the passive state. *Journal of The Electrochemical Society* **139**, 3434-3449 (1992).
- 73 Matin, S. *et al.* Use of Multielectrode Arrays and Statistical Analysis to Investigate the Pitting Probability of Copper. Part I: The Effect of Chloride. *Journal of The Electrochemical Society* **169**, doi:10.1149/1945-7111/ac78d3 (2022).

- 74 Mao, F., Dong, C., Sharifi-Asl, S., Lu, P. & Macdonald, D. D. Passivity breakdown on copper: Influence of chloride ion. *Electrochimica Acta* **144**, 391-399, doi:10.1016/j.electacta.2014.07.160 (2014).
- 75 Biesinger & C., M. Advanced analysis of copper X-ray photoelectron spectra. *Surface and Interface Analysis* **49**, 1325-1334, doi:10.1002/sia.6239 (2017).
- 76 F. King, Lilja, C., Pedersen, K., Pitkänen, P. & Vähänen, M. An update of the state-of-the-art report on the corrosion of copper under expected conditions in a deep geologic repository. Report No. TR-10-67, (SKB, 2010).
- 77 Macdonald, D. D. The history of the Point Defect Model for the passive state: A brief review of film growth aspects. *Electrochimica Acta* **56**, 1761-1772, doi:10.1016/j.electacta.2010.11.005 (2011).
- 78 Kunze, J., Maurice, V., Klein, L. H., Strehblow, H.-H. & Marcus, P. In situ STM study of the effect of chlorides on the initial stages of anodic oxidation of Cu(111) in alkaline solutions. *Electrochimica Acta* **48**, 1157-1167, doi:10.1016/s0013-4686(02)00826-5 (2003).
- 79 Nishikata, A., Itagaki, M., Tsuru, T. & Haruyama, S. Passivation and its stability on copper in alkaline solutions containing carbonate and chloride ions. *Corrosion Science* **31**, 287-292 (1990).
- 80 Baes, C. F. & Mesmer, R. E. (John Wiley & Sons, New York, 1976).
- 81 Sharma, V. K. & Millero, F. J. The oxidation of Cu (I) in electrolyte solutions. *Journal of Solution Chemistry* **17**, 581-599 (1988).
- 82 King, F. Corrosion of copper in alkaline chloride environment. Report No. TR-02-25, (Swedish Nuclear Fuel and Waste Management Co, 2002).